

Full length article

Synthetic bone: Design by additive manufacturing

D. Barba^{a,d}, E. Alabort^c, R.C. Reed^{a,b,*}^a Department of Materials, University of Oxford, Parks Road, Oxford OX1 3PH, United Kingdom^b Department of Engineering Science, University of Oxford, Parks Road, Oxford OX1 3PJ, United Kingdom^c OxMet Technologies, 15, Oxford Industrial Park, OX5 1QU, United Kingdom^d School of Aeronautics and Space Engineering-ETSAE, Polytechnic University of Madrid, 28040 Madrid, Spain

ARTICLE INFO

Article history:

Received 1 April 2019

Revised 22 July 2019

Accepted 26 July 2019

Available online 5 August 2019

Keywords:

Lattices

3D-printing

Lattice

Biomaterial

Implants

Osseointegration

ABSTRACT

A broad range of synthetic trabecular-like metallic lattices are 3D printed, to study the extra design freedom conferred by this new manufacturing process. The aim is to propose new conceptual types of implant structures for superior bio-mechanical matching and osseointegration: synthetic bone. The target designs are 3D printed in Ti-6Al-4V alloy using a laser-bed process. Systematic evaluation is then carried out: (i) their accuracy is characterised at high spatial resolution using computed X-ray tomography, to assess manufacturing robustness with respect to the original geometrical design intent and (ii) the mechanical properties – stiffness and strength – are experimentally measured, evaluated, and compared. Finally, this new knowledge is synthesised in a conceptual framework to allow the construction of so-called implant design maps, to define the processing conditions of bone tailored substitutes, with focus on spine fusion devices. The design criteria emphasise the bone stiffness-matching, preferred range of pore structure for bone in-growth, manufacturability of the device and choice of inherent materials properties which are needed for durable implants. Examples of the use of such maps are given with focus on spine fusion devices, emphasising the stiffness-matching, osseointegration properties and choice of inherent materials properties which are needed for durable implants.

Statement of Significance

We present a conceptual bio-engineering design methodology for new biomedical lattices produced by additive manufacturing, which addresses some of the critical points in currently existing porous implant materials. Amongst others: (i) feasibility and accuracy of manufacturing, (ii) design to the elastic properties of bone, and (iii) sensible pores sizes for osseointegration. This has inspired new and novel geometrical latticed designs which aim at improving the properties of intervertebral fusion devices. In their fundamental form, these structures are here fabricated and tested. When integrated into medical devices, these concepts could offer superior medical outcomes.

© 2019 Acta Materialia Inc. Published by Elsevier Ltd. This is an open access article under the CC BY-NC-ND license. (<http://creativecommons.org/licenses/by-nc-nd/4.0/>)

1. Introduction

Bone is a complex porous bio-material with non-homogeneous anisotropic properties which supports organs, muscles and other body tissues [1,2]. Its structure – and therefore its mechanical properties – are the result of its required functionality: porosity and fibrous direction of the bone tissue are controlled by biological processes that tailor the topology of the local tissue to the mechanical requirements [1]. This leads to a wide range of porosities, mechanical properties and anisotropy within the same bone – all

of them optimised for its optimal macroscopic functionality [3,4]. Even wider are the changes between different parts of the bone (trabecular or cortical), the age, sex, loading direction or anatomical site [5–8]. It is well known that this macroscopic structure is in local mechano-biological equilibrium [1,9,2]: when local bone tissue is not stressed, the local flow of nutrients is stopped. This leads to retraction of the bone tissue. Local mechanical stimulus is therefore needed to keep bone tissue alive and healthy. This can only be achieved when the vascular system hosted by the bone porous structure transports a continuous flow of nutrients [10,11].

These two aspects (mechanical stimulus and nutrient support for osseointegration) become critical for optimal bone implant design. Implants are used when bone tissue needs to be replaced by

* Corresponding author.

E-mail address: roger.reed@eng.ox.ac.uk (R.C. Reed).

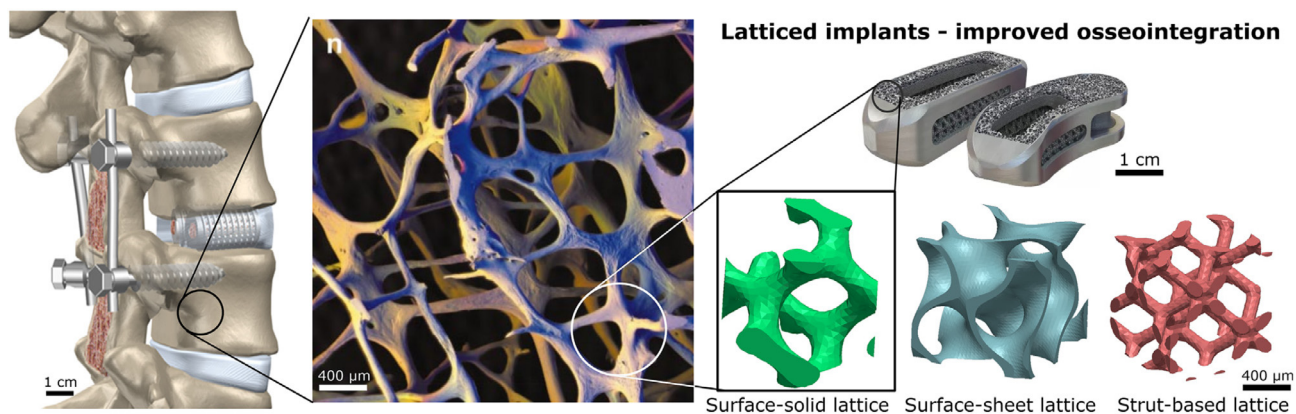


Fig. 1. (Left) Spine with implanted inter-disk metal device; (center) trabecular bone structure (adapted from Hansma et al. [79]); (right) porous spinal implant device on top (adapted from Captiva [24]) and three different types of lattice topologies at the bottom. The surface-based skeleton type lattice is selected for this work.

synthetic medical devices due to biological problems (osteoporosis, cancer, fracture...) [12–14]. Titanium alloys are the preferred option in long-term load-bearing osseointegrated bone implants due to a combination of relatively low elastic modulus, good biocompatibility, exceptional corrosion resistance, and suitable fatigue strength when compared with other biomaterials such as cobalt-alloys, steels or PEEK polymers [15,16]. However, the stiffness of solid Ti alloys – although lower than other alloys – still exceeds the stiffness of bone by an order of magnitude. This leads to the so-called stress shielding phenomenon [17,9]; when surrounding bone is not stressed due to a stiffness mismatch between the implant and the bone. The lack of long-term strain stimulus in the bone can lead to bone resorption. This is not desirable [10,9]. In addition to the shielding problem, the impossibility of vascularisation in solid implants leads to a deficit of nutrients to the surrounding bone [11].

Advanced manufacturing (AM) has opened the door for a new class of porous latticed implants which can circumvent many of these problems [16,18]. An example of a porous medical device fabricated by AM is presented in Fig. 1, a latticed intervertebral fusion device which is used in this work as the design target. This kind of porous materials are known as meta-materials and they can have tailored mechanical properties. The internal structure of pores of these meta-materials allows one to simultaneously: (1) lower the stiffness to levels suitable for bone applications and (2) host the network of nutrient flow needed to keep the bone healthy in a load bearing state [11]. Several techniques have been developed recently for lattice manufacturing. For example, freeze-casting [19], 3D fiber deposition [20], space holder techniques [21] or powder sintering processes [22]. However, the use of these techniques often introduces critical limitations such as small porosity levels, coarse control of size, shape, and distribution of the pores, or even presence of impurities. Recently, additive manufacturing (AM) has allowed accurate control of the internal pore structure of porous architecture, thus allowing complex geometries to be manufactured with repeatability. These kind of additive manufactured lattices are gaining a great interest in the biomedical field [23–25]. Among the different additive manufacturing techniques, selective laser melting (SLM) can be regarded as a very promising route for medical devices due to its versatility, high-precision and accuracy, surface finish, and proven structural integrity [26,27]. The SLM process is used in this work. SLM is believed to be the best choice for the small features (<500 μm) which are typically present in spinal fusion implant devices which are the focus of this study.

Among all the many possible lattice geometries, three main groups can be identified which are based upon the principles of computational geometry, (see Fig. 1). First, lattices based on beams

[28–30]. Second, lattices based on triple periodical minimal surfaces (TPMS) with added thickness [31,32]. Finally, there are lattices derived from TPMS in a skeleton fashion [33,34] (see Fig. 2). For bone-substitute applications, TPMS skeletal surfaces are known to present some advantages over strut- and sheet-TPMS-based lattices. These are: (i) a single cell domain with improved pore connectivity – as compared to TPMS sheet lattices; and (ii) smoother wall curvature in contrast to strut-base lattices – this reduced curvature is linked to improved bone in-growth [18,35]. For this reason we have chosen to focus on TPMS skeletal surfaces in this work. However, there is a vast library of TPMS topologies that one may use. Moreover, the wide range of unit cells, porosities and thicknesses achievable by SLM makes design optimisation a complex challenge. It is evident that a range of geometries and porosities with good manufacturability, good mechanical matching with the surrounding bone, and that include a preferred range of pore sizes to host bone ingrowth [36] must exist. These three critical aspects have been widely studied in the literature, albeit rather independently:

- **Geometry → Manufacturability:** Several authors have studied the manufacturability of different lattice designs and porosities. Van Bael et al. [37] presented a detailed iterative study aiming to reduce the manufacturing errors on pore sizes, strut thicknesses, porosities, and surface area in metal lattices with great results. In a further work, Van Bael et al. [35] studied the deviation between designed and manufactured pore sizes using μ -CT scans and optical microscopy showing important deviations (10–20%) for some geometries. They also showed good pore inter-connectivity values. However, this study focused on rather large unit cells (≈ 2 mm) – excessive for optimal osseointegration. Wang et al. [38] proposed a series of design rules to ensure optimal lattice processability. These include critical strut angles and minimum lattice sizes depending on the processing capabilities. Yan et al. [27] studied the spatial deviations of AM-manufactured Gyroid-skeleton lattice made by Ti-6Al-4V with large unit cells (4–7 mm) – deviations of 200 μm or less were reported. Tan et al. [39] proposed a series of theoretical design rules for lattices which accounted for manufacturability limitations. Strut thicknesses below 200 μm qualified as non-manufacturable by SLM processes. Melancon et al. [40] presented a complete study on the manufacturability of tetrahedral and octahedral strut-based unit cells. They presented manufacturability maps based on geometrical experimental studies determining the deviation from the ideal pore size, strut thickness and porosity.

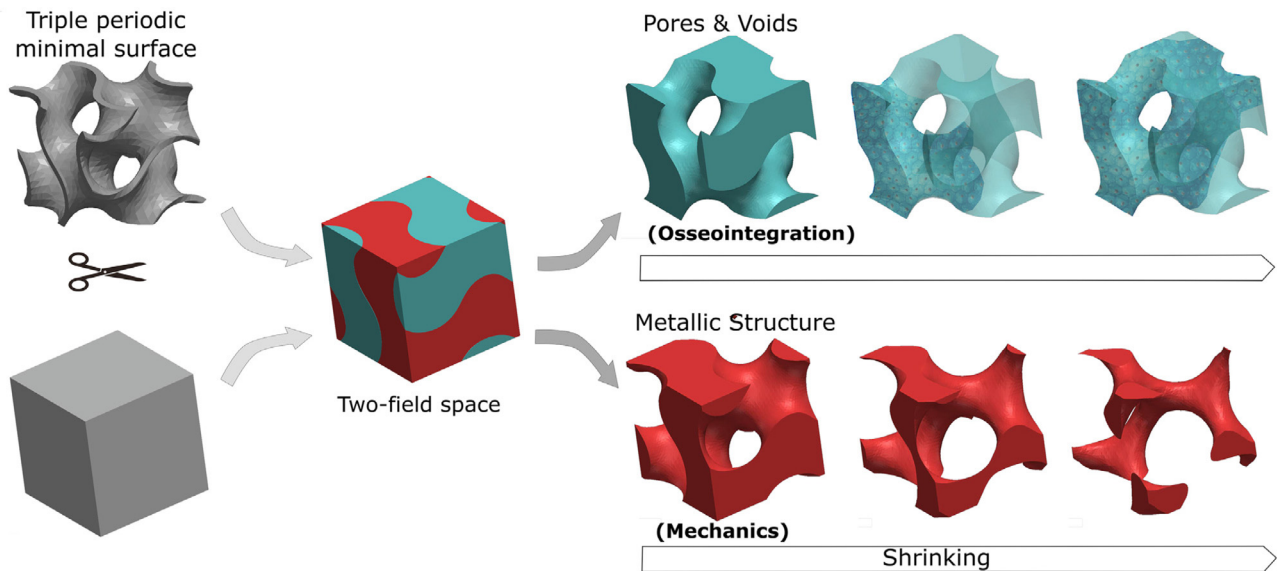


Fig. 2. Diagram of the construction of TPMS-based skeleton type lattices and its connection with the mechanical and osseointegration properties. The build space is split in 2 by the TPMS. One side is filled with material and the other is left free for bone ingrowth. The target porosity is achieved by shrinking or expanding the material volume.

- Geometry → Mechanical response:** The foam theory developed by Ashby, Gibson and others [41,42] in the 90s sets the basis for the complex lattice theory development which followed. Indeed, many studies have linked lattice mechanical properties to their geometry and porosity [27,43,28,39,44] – these are critical for lattice optimisation and bone stiffness matching. Among them, Cheng et al. [28] presented a comprehensive mechanical study of the micro-deformation mechanisms underlying the different in mechanical responses. Yang et al. [27] studied the mechanical performance of Gyroid- and Diamond-based TPMS following Ashby's relations. Xu et al. [44] focused his attention on another characteristic of these structures, the high anisotropy of some of the lattice structures. By means of computational models, they described the anisotropic behaviour of different strut-based lattices and proposed procedures to tailor this anisotropy. Egan et al. [29] studied the design of strut-based lattices using computational tools to find the correct values of porosity and unit cell size for bone applications. Bobbert et al. [31] designed a comprehensive experimental campaign to address the mechanical response and permeability of 4 different sheet-based TPMS (primitive, IWP, Gyroid, Diamond) as function of porosity. Tan et al. [39] provided a magnificent review of the geometry-to-mechanical relationship of strut-based lattices for orthopedic applications. Zhang et al. [43] studied complex strut-based lattice structures with variable local porosities to match the stiffness of the different parts of the bone (cortical bone, transition zone and bone marrow). They rationalised computationally the mechanical response of the compound lattice. Finally, Al-Ketan et al. [32] performed a vast experimental study on the 3 different type of lattices introduced previously in Fig. 1: 3 geometries of each type and 4 different porosities – sheet-based TPMS showed superior specific strength. Melancon et al. [40] developed a combined experimental and modelling study on the mechanical response of tetrahedral and octahedral strut-based unit cells.
- Geometry → osseointegration:** Finally, several authors have studied the effect of geometry (pore size and lattice cell) in osseointegration performance [45,43,46,35]. Warnke et al. [45] studied the effect of pore size (450–1200 μm) on osteoblast growth – pores below 600 μm are suitable for complete tissue in-growth. Zhang et al. [43] studied experimentally

the effect of different pore sizes on the permeability of the lattice, linking it to the nutrient transport needed for bone ingrowth). They discovered a direct positive correlation between pore size/porosity and permeability which follows an asymptotic trend. Taniguchi et al. [46] extended this study to in vivo conditions analysing the effect of the pore size (300, 600 and 900 μm) on the inter-facial strength between bone and implant. They found that 600 μm pore sizes were the optimal for the long-term bone ingrowth and therefore the so-called union strength. Van Bael et al. [35] studied the effect of different pore geometries (triangular, quasi-circular and squared) and pore sizes (500 μm and 1000 μm) on the cell living densities and on their differentiation rates. They found that smaller circular pores – 500 μm – improved initial cell attachment but larger pores – of $\approx 1000 \mu\text{m}$ – are more likely to host living cells after 14 days. Fukuda et al. [47] showed that porous channels of 500 μm provide the best osseointegration – within the studied range of 500–1200 μm . Wu et al. [48] found that porous structures made of Ti-6-Al-4V with average pore size in the range of 700 μm present good osseointegrative properties, better than the equivalent structure made of PEEK. Gotz et al. [49] observed a minimum pore size of 200 μm to obtain optimal osseointegration, and minor changes above this value. Furthermore, a wide bunch of studies has set a minimum pore size of 250–300 μm to allow a full bone osseointegration with the porous lattice (including vascularisation) [50–53]. In terms of the superior limit, several studies mentioned before inferred a drop of osseointegrative properties for pore sizes above 500–600 μm [47,46,45]. These studies are the basis of the low and high pore size requirements introduced in the discussion section.

Despite great efforts to study the link between lattice design, manufacturability, mechanical properties and osseointegration, the available literature does not relate them directly: there is a disconnection between the topics. There is need for a unified holistic engineering study that combines the three main aspects: with the aim of geometrical optimisation for implant design. With this in mind, the purpose of this work is to develop a versatile conceptual design framework of manufacturable implants with combined optimal mechanical properties and a suitable pore size distribution for osseointegration. For this purpose, the manuscript analyses a

Table 1

Mathematical definition of the different surfaces studied in this work. *The Neovius surface is a modified version by Simpleware [56] of the original surface.

TPMS	Surface equation
Schwarz IWP	$\sin(2\pi x) \cdot \sin(2\pi y) \cdot \sin(2\pi z) + \sin(2\pi x) \cdot \cos(2\pi y) \cdot \cos(2\pi z) + \cos(2\pi x) \cdot \sin(2\pi y) \cdot \cos(2\pi z) + \cos(2\pi x) \cdot \cos(2\pi y) \cdot \sin(2\pi z)$
Neovius*	$3(\cos(2\pi x) + \cos(2\pi y) + \cos(2\pi z)) + 4\cos(2\pi x)\cos(2\pi y)\cos(2\pi z)$
Schoen Gyroid	$\sin(2\pi x) \cdot \cos(2\pi y) + \sin(2\pi y) \cdot \cos(2\pi z) + \sin(2\pi z) \cdot \cos(2\pi x)$
Schwarz Diamond	$\sin(2\pi x) \cdot \sin(2\pi y) \cdot \sin(2\pi z) + \sin(2\pi x) \cdot \cos(2\pi y) \cdot \cos(2\pi z) + \cos(2\pi x) \cdot \sin(2\pi y) \cdot \cos(2\pi z) + \cos(2\pi x) \cdot \cos(2\pi y) \cdot \sin(2\pi z)$

variety of TPMS-skeleton geometries and porosities built via SLM using Ti-6Al-4V with focus on interbody spine fusion devices. It is important to notice importance of targeting an specific anatomical site for this study due to the variety of mechanical properties found in different bones. The paper is structured as follows; (1) the manufacturability of the different latticed structures is addressed by means of 3D quantitative analysis; (2) the mechanical performance of the different lattices is studied experimentally to determine their mechanical stiffness and compressive strength; (3) the geometrical aspects related to the osseo-integration capabilities – i.e., pore size and porosity – are investigated; and (4) mathematical relations arising from this three-pronged conceptual study are used to build lattice design maps targeting intervertebral fusion devices. These maps are used to propose optimal design spaces for biomedical implants with different materials. It is important to note that although we point in this design exercise to intervertebral fusion devices, the framework presented here is generic and can be applied to any bone replacement device which require certain mechanical properties and osseointegrative properties. We have chosen intervertebral fusion devices as a design exercise because they present currently a combination of mechanical and osseointegrative requirements that are important to satisfy for optimal results.

2. Methods

In the following section, the different techniques, experimental methods and computational procedures used in this study are detailed.

2.1. Design and manufacturing of the lattices

Two main different group of lattices can be defined: strut-based lattices [28–30] and surface-based lattices [31–34]. The first ones are formed by beam-like elements (see Fig. 1) combined at the nodes. The latter are defined by mathematical surfaces. Strut-based lattices present several advantages: they are easier to process and manufacture, and they are available in most design and AM software packages [54,55]. However, for biomedical applications, where osseo-integration and cell growth is critical, surface based lattices have demonstrated to be a better option than struts due to their smoother curvature [18,35]. Among these surfaces, there is a special type called triple-periodical minimum surfaces (TPMS) with zero mean curvature. These present improved cell attachment and better osseo-integration than standard edged surfaces [18,35]. There are two ways to construct lattices using TPMS: (i) by adding thickness to the surface as shown in Fig. 1; (ii) by assuming that the TPMS is the frontier between the solid material and the empty space as described in Fig. 2. The latter provides lattices with a unique cell growth domain with obvious advantages for osseo-integration – this was selected in the present study.

Four different TPMS are considered in this study: Schwarz IWP, Neovius, Schoen Gyroid and Schwarz Diamond. The mathematical

expression for each of the surfaces are detailed in Table 1. For each of the lattice geometries, four different solid fractions are considered (15%, 25%, 50% and 85%) to study the effect of porosity on the manufacturability and mechanical properties. The 16 different geometries (Four TPMS \times Four relative densities) are detailed in Fig. 3.

Cylinders of 12 mm diameter and 12 mm height were filled with the different unit cells described in Fig. 3 using Synopsis Simpleware [56]. A unit cell size of 1 mm is selected for this study giving approximately 200–600 μm pore size for porosities of 20–40% (the optimal pore size agreed in the literature [39,43]). This gives around 10 unit cells per direction to assure a representative volume element (RVE) contained in the specimen.

The tested specimens were built using a Renishaw AM400 machine with a modulated 200 W ytterbium fibre laser. The power fed into the machine was a plasma atomised Ti-6Al-4V provided by Renishaw. Ti-6Al-4V was chosen in this study due to its extensive use in biomedical devices, specially fusion cage devices even if the Vanadium contained in the alloy is believed cytotoxic. However, this conceptual framework can be applied to other metals. The processing parameters for the additive manufacturing process were optimised for highly-dense conditions – these are detailed in Table 2.

The deviation between the designed solid fraction and the real one was measured using the weight measurements of the manufactured lattices. The set of lattices were weighted and their relative density was calculated following

$$\%_{\text{solid fraction}} = \frac{W_{\text{sample}} / \rho_{\text{Ti6Al4V}}}{V_{\text{sample}}} \quad (1)$$

were W_{sample} and V_{sample} are the weight and volume of the sample respectively, and ρ_{Ti6Al4V} is the theoretical density of Ti-6Al-4V (4.43 g/cm³).

The manufacturability study is extended using micro computer tomography (μ CT) analysis. CT scans of the 16 different lattices were acquired using a μ CT scanner (Benchtop CT 160Xi, X-Tek) with a 27 mm resolution at 120 kV voltage and 182 mA current. Simpleware Scan-IP [56] was used to reconstruct the 3D models of the lattice structures using the 2D slice image data of the whole specimens. Then, the deviation between the manufactured and the ideal surfaces was quantified.

2.2. Mechanical testing of the lattices

Compression tests were performed on the cylindrical 3D printed specimens introduced previously. For this purpose, an Instron servo-electric machine was used. The frame is equipped with compression grips and SiC disc anvils (50 mm diameter and 15 mm thick) to transfer the load from the specimen to the grip fixture. The specimens were compressed at a constant strain rate of 10^{-2} s^{-1} . The displacement of the grips and the deformation of the lattices were monitored using digital image correlation (DIC).

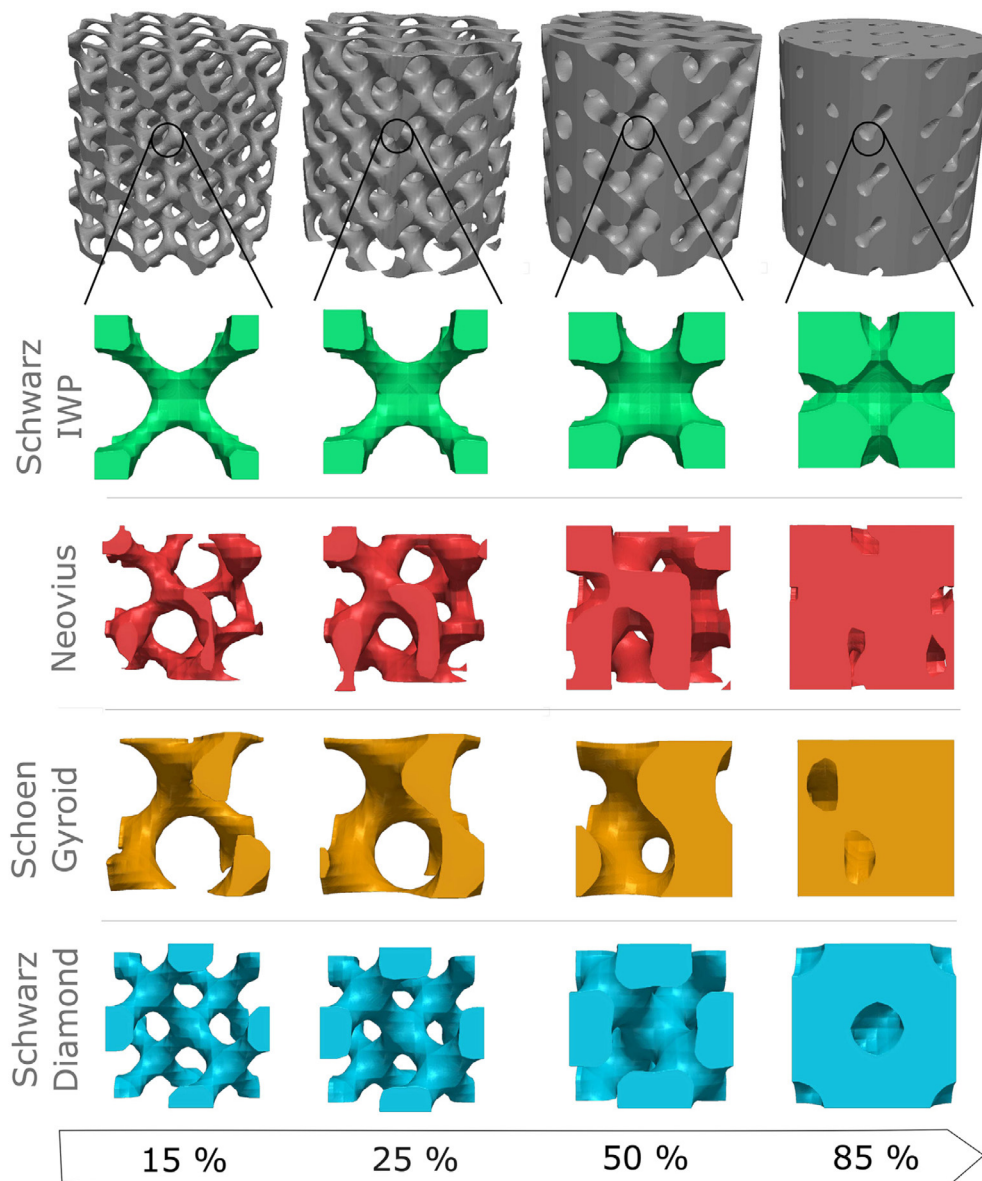


Fig. 3. Set of geometries and porosities selected for the present study. The set is composed by four TPMS-derived skeleton geometries (IWP, Neovius, Schoen Gyroid, and Diamond) and four different solid fractions (15, 25, 50, and 85%).

Table 2

Processing parameters for additive manufacturing of the samples.

Ti-6Al-4V	Hatch parameters	Border parameters
Layer thickness	30 μm	30 μm
Laser Power	200 W	100 W
Point distance	55 μm	45 μm
Hatch distance	65 μm	65 μm
Exposure time	50 μs	40 μs

The tests were stopped after 50% engineering strain. Three repeats were performed for each condition – a total of 48 specimens were tested to ensure repeatability.

2.3. Measurement of pore-size distributions

The pore size distribution of the different lattices was measured as a function of the porosity and the unit cell size. For each topology, 10 \times 10 unit cells were computed. The pore network of each of

the lattices were analysed using the segmentation, reconstruction and analysis software Avizo 9.5.0 [57] following Fig. 4. The throat and pore size distribution were extracted, thus allowing estimation of an average pore size.

3. Results

3.1. Effect of lattice design on manufacturability

In this section, we characterise the manufacturability of the medical lattices under study. The section is structured as follows: (1) first the deviation from the macroscopic design solid fraction is presented and some causes for these deviations are introduced; (2) the local geometrical deviation is studied using CT-tomography techniques. The results presented here are the basis for the manufacturability criteria presented later in the discussion.

The measured solid fractions are presented in Fig. 5 as column bars and compared against their ideal values. For Neovius, Gyroid and Diamond, the target porosity is matched within rea-

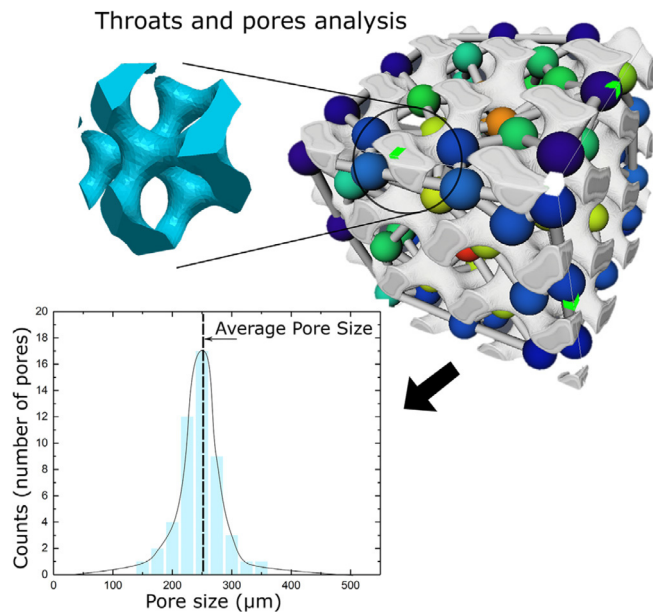


Fig. 4. Analysis of the pore size structure from a given lattice structure and example of the pore size distribution extracted from this analysis.

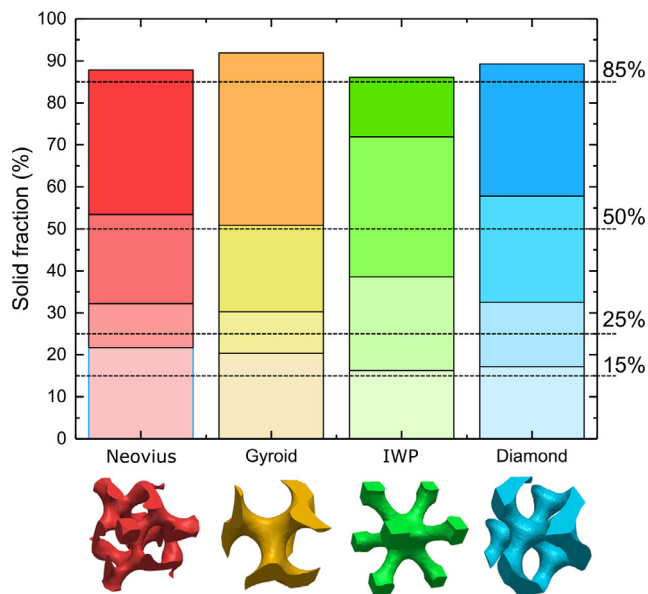


Fig. 5. Measured value of the measured solid fraction for the 4 different geometries using the weight-volume method. The horizontal dashed-lines indicate the targeted solid fractions.

sonable accuracy. However, the IWP geometry shows more pronounced deviations for mid-porosities (25–50%) – this might be associated with the specific manufacturing difficulties related with the 8-struts forming its unit cell. For all the cases, the solid fraction of the manufactured lattices is higher than the target values. These findings are further rationalised in the geometrical study presented next.

High manufacturing accuracy is crucial in biomedical lattices. Small changes in the geometry can lead to significant variations in their mechanical properties. For this reason the local deviations of the geometry are studied using tomography techniques. The ideal unit-cell lattice geometry, a representative unit cell of a reconstructed manufactured unit cell, and the deviation between both are presented in Figs. 6–9 for the Neovius, Gyroid, IWP and Diamond geometries respectively. Results show that first two –

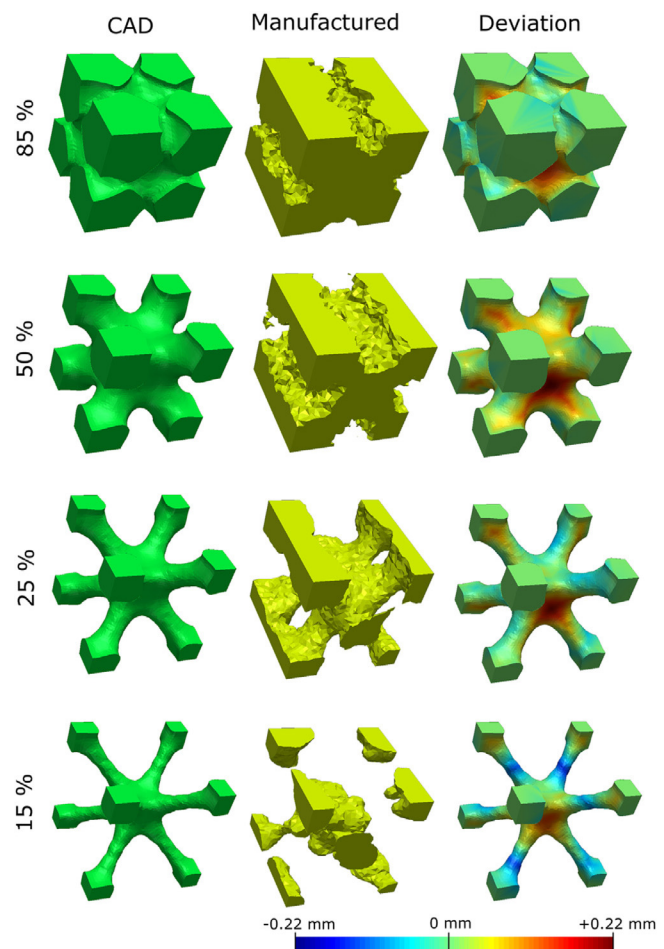


Fig. 6. Comparative study of geometrical accuracy of the AM lattice for the IWP unit cell. The first column shows the ideal lattice, the middle column the reconstruction of the real lattice from computer tomography analysis and the third column the comparison between both. Red regions indicate excess of materials and blue regions lack of material.

Neovius and Gyroid unit-cells – are manufactured with reasonable accuracy – at least for low and mid range porosities (15–50% solid fractions). IWP and Diamond geometries show higher deviation. Both geometries show unconnected struts – these will affect the structural performance. This is linked with the presence of very thin features. These observations are used to propose a printability criterion. This is based on a minimum effective strut thickness. A common point between topologies is that at lower solid fractions (15%) there is a consistent lost of material with respect to the computed geometry (see blue regions in IWP and in Diamond geometries in Figs. 8 and 9). On the other side, at higher solid fractions (50%–85%) there is an excess of bulk material in all geometries (red regions in Figs. 6–9). This is caused by metal powder trapped and sintered within the smallest cavities. This is a serious concern for orthopaedics – small metal particles getting into the blood stream can be highly toxic [58–60]. Although Ti-6Al-4V does not present major problems in terms of toxicity, vanadium particles in the body are not desirable due to its high cytotoxicity [61]. Moreover, large doses of loose Ti-6Al-4V powder can also cause cytotoxicity. Therefore, solid fractions above 50% are considered inappropriate in this study for bio-medical applications. This limit is further supported by the high stiffness in lattices with > 50% solid fraction.

Fig. 10 shows the statistical geometrical deviation for all the manufactured lattices – i.e. mean deviation and amount of mate-

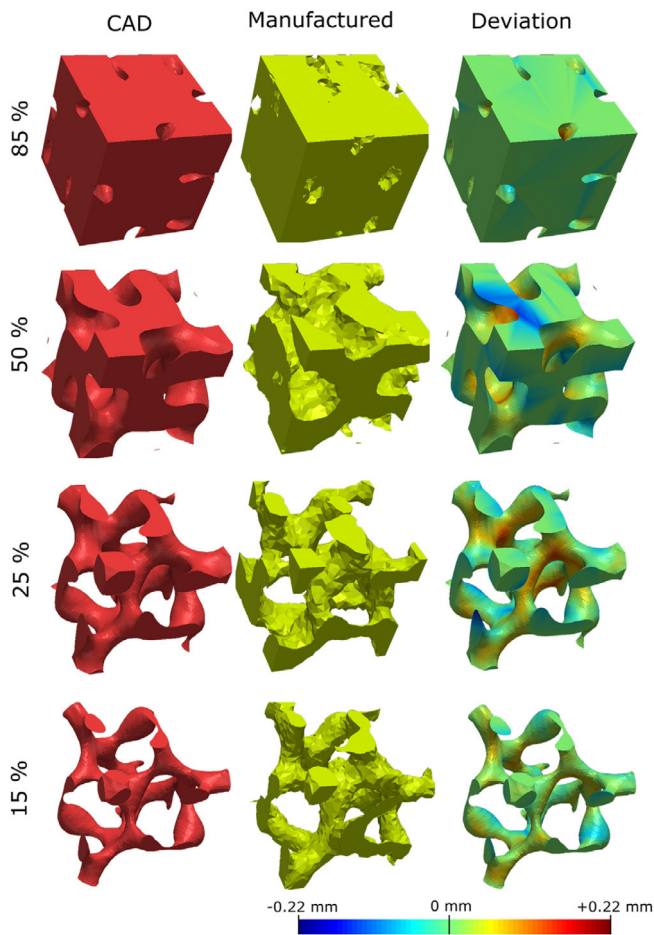


Fig. 7. Comparative study of geometrical accuracy of the AM lattice for the Neovius unit cell. The first column shows the ideal lattice, the middle column the reconstruction of the real lattice from computer tomography analysis and the third column the comparison between both. Red regions indicate excess of materials and blue regions lack of material.

rial above certain threshold deviation). The mean square error in Fig. 10a – which accounts for both excess and lack of material – shows similar behaviour for all geometries at mid-porosities (25–50% s.f.). For highly porous lattices, *i.e.* 15% s.f., Diamond and IWP show the highest deviation. For highly dense lattices, *i.e.* 85% s.f., the Diamond geometry shows the worst accuracy. Fig. 10b–c show that the absolute deviation from the mean square error is split in positive (material excess) or negative (material missing) deviations. When considering a threshold error of 100 μm (10% of the 1 mm unit cell), one observes that most of the error is due to material excess. IWP 15% s.f. is the exception: there are large areas with missing material. This is in agreement with results shown in Fig. 6. The rest of 15–50% s.f. geometries show relatively small errors. However, when considering a threshold error of 50 μm , all the lattices present larger deviations. As a conclusion, all the lattices present accuracy errors – more commonly excess of material – but for the case of Neovius, Gyroid and Diamond, these deviation are smaller (within $\leq 50 \mu\text{m}$) (see Fig. 10).

3.2. Effect of lattice design on mechanical behaviour

In this section, a series of mechanical tests are performed to evaluate the mechanical behaviour of the different lattices as a function of geometry and porosity. Then, the elastic anisotropy of each lattice type is studied computationally. Finally, a series of mathematical relationships for the mechanical performance of

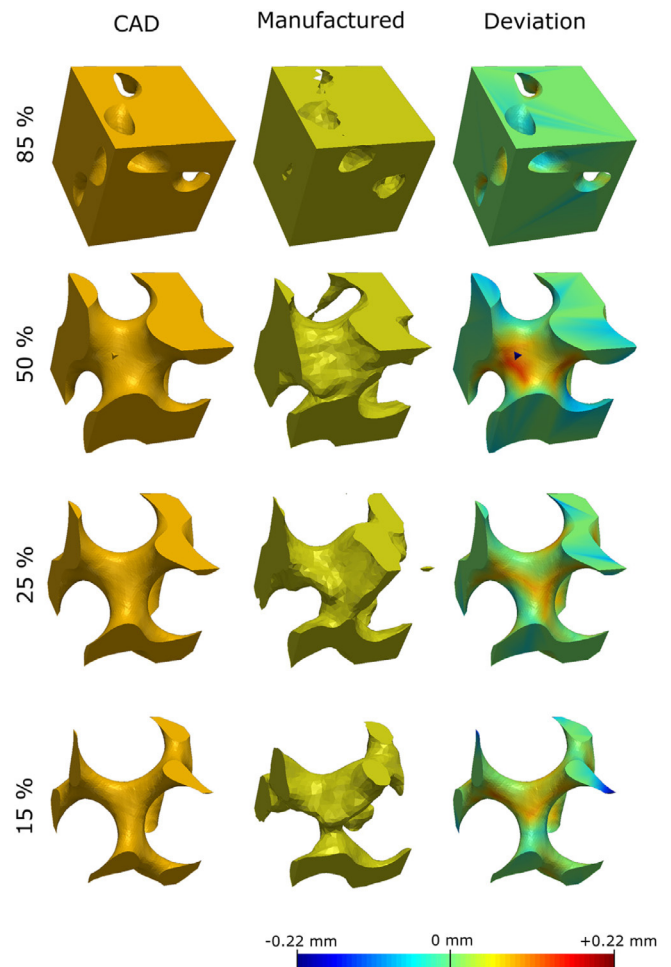


Fig. 8. Comparative study of geometrical accuracy of the AM lattice for the Schoen Gyroid unit cell. The first column shows the ideal lattice, the middle column the reconstruction of the real lattice from computer tomography analysis and the third column the comparison between both. Red regions indicate excess of materials and blue regions lack of material.

the lattice (stiffness and compressive strength) are derived using Ashby's theory.

Fig. 11 shows the compressive behaviour of the different lattices in the form of stress-strain curves. Statistical values for the elastic modulus, the yield stress, the maximum stress and the plateau stress are presented in Table 4. The fracture mode (if present) and the presence of crushing (mechanical oscillations of the stress) are also indicated in this Table. The stages of deformation observed in Fig. 11 are in agreement with other experimental studies in the literature [31,11]: (i) an initial elastic loading stage followed by (ii) a yielding of the structure and a plateau region (with a plateau stress or oscillatory behaviour) and finally (iii) a stress increase due to the densification of the porous structure due to crushing. Some lattices do not exhibit this third stage due to brittle fracture (*e.g.* IWP-25% s.f.). For all the geometries, the peak stress and the stiffness increase as the solid fraction increases. The following particular behaviour is observed for each of the relative densities:

- **15% Solid fraction:** Neovius geometry presents a flat-type plateau while IWP and Gyroid topologies present oscillation crushing before densifying. This difference can be caused by the wider variety of "elemental strut" orientations present in the Neovius topology (see Fig. 3). IWP exhibits poor mechanical properties due to the manufacturing challenges highlighted previously. The densification rate is higher for the Gyroid geometry.

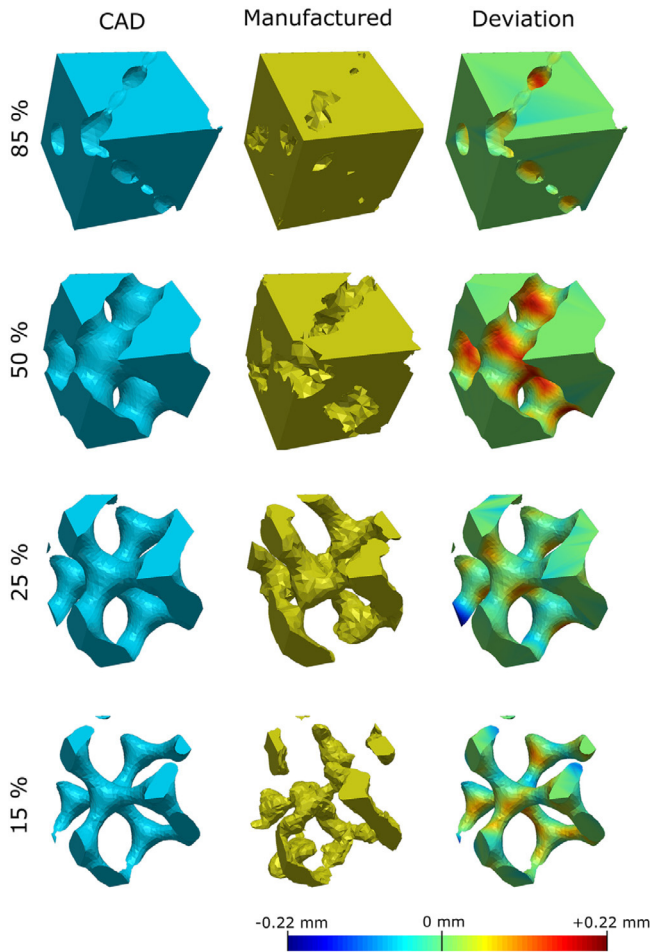


Fig. 9. Comparative study of geometrical accuracy of the AM lattice for the Diamond unit cell. The first column shows the ideal lattice, the middle column the reconstruction of the real lattice from computer tomography analysis and the third column the comparison between both. Red regions indicate excess of materials and blue regions lack of material.

- **25% Solid fraction:** IWP shows a higher increase in stress level which leads to brittle fracture at low strains (undesirable for medical devices). IWP, Diamond, and Gyroid present an initial stress oscillation regime before densifying (for the Gyroid geometry the oscillations vanish sooner when compared to 15% s.f.). Neovius presents continuous densification after yielding followed by a flat plateau at high strains ($\varepsilon > 35\%$).
- **50% Solid fraction:** Neovius, Gryoid, and Diamond present similar responses – strong densification after initial yielding. In the case of IWP, only the elastic regime and the initial stage of the plastic regime is captured – the maximum load cell value was reached (100 kN).
- **85% Solid fraction:** only the elastic response is captured. Diamond topology shows the highest stiffness followed by Neovius, IWP, and Gyroid respectively.

Figs. 12 and 13 employ Ashby's diagram to summarise the mechanical behaviour explained above. The stiffness and the yield stress are shown as a function of the relative density. Following Ashby's theory, the experimental points are fitted to linear expressions of the form:

$$\frac{E^*}{E_s} = C_E \cdot \left(\frac{\rho^*}{\rho_s} \right)^{m_E} \quad (2)$$

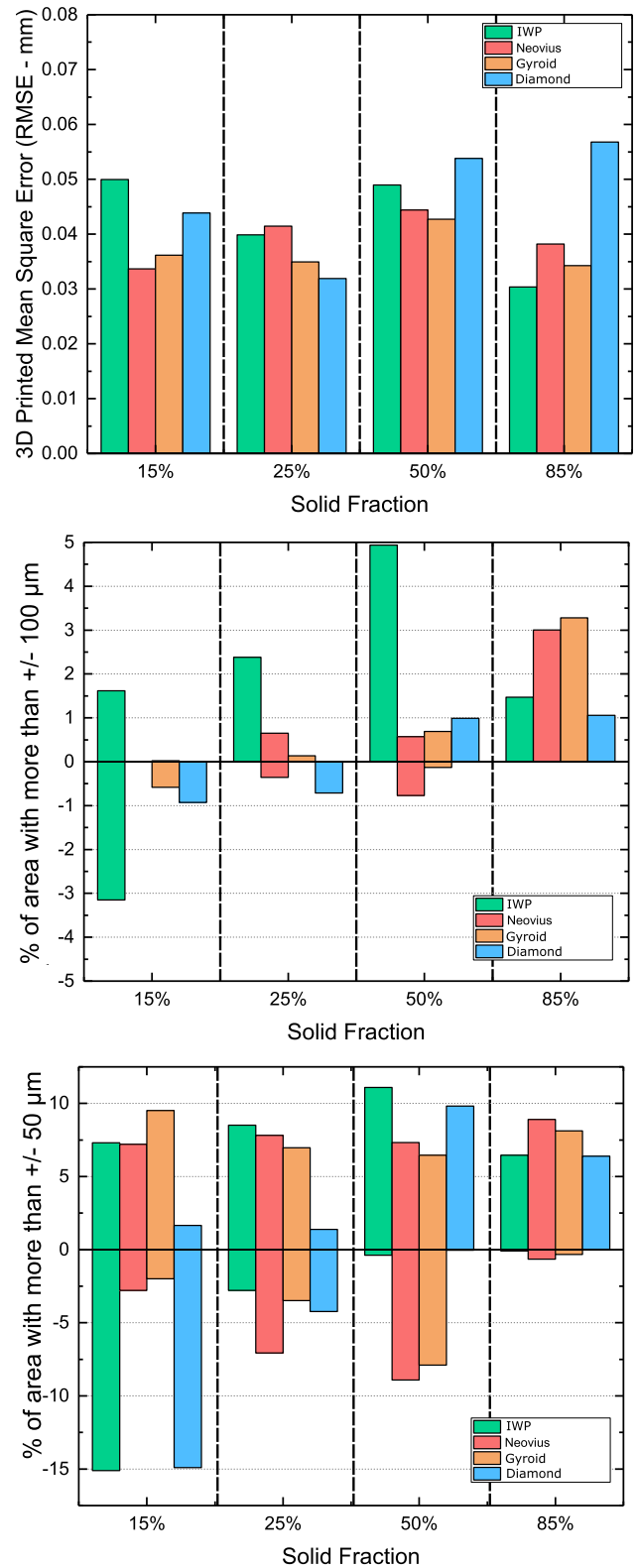


Fig. 10. Statistical values for the geometrical error analysis presented in Figs. 6–9.

(a) Indicates the mean square error $\varepsilon_{sq} = \sqrt{\sum_i (\mathbf{x}_{\text{real}} - \mathbf{x}_{\text{ideal}})^2}$; (b) amount of area with a deviation larger than $100 \mu\text{m}$ from the reference surface; (c) amount of area with a deviation larger than $50 \mu\text{m}$ from the reference surface.

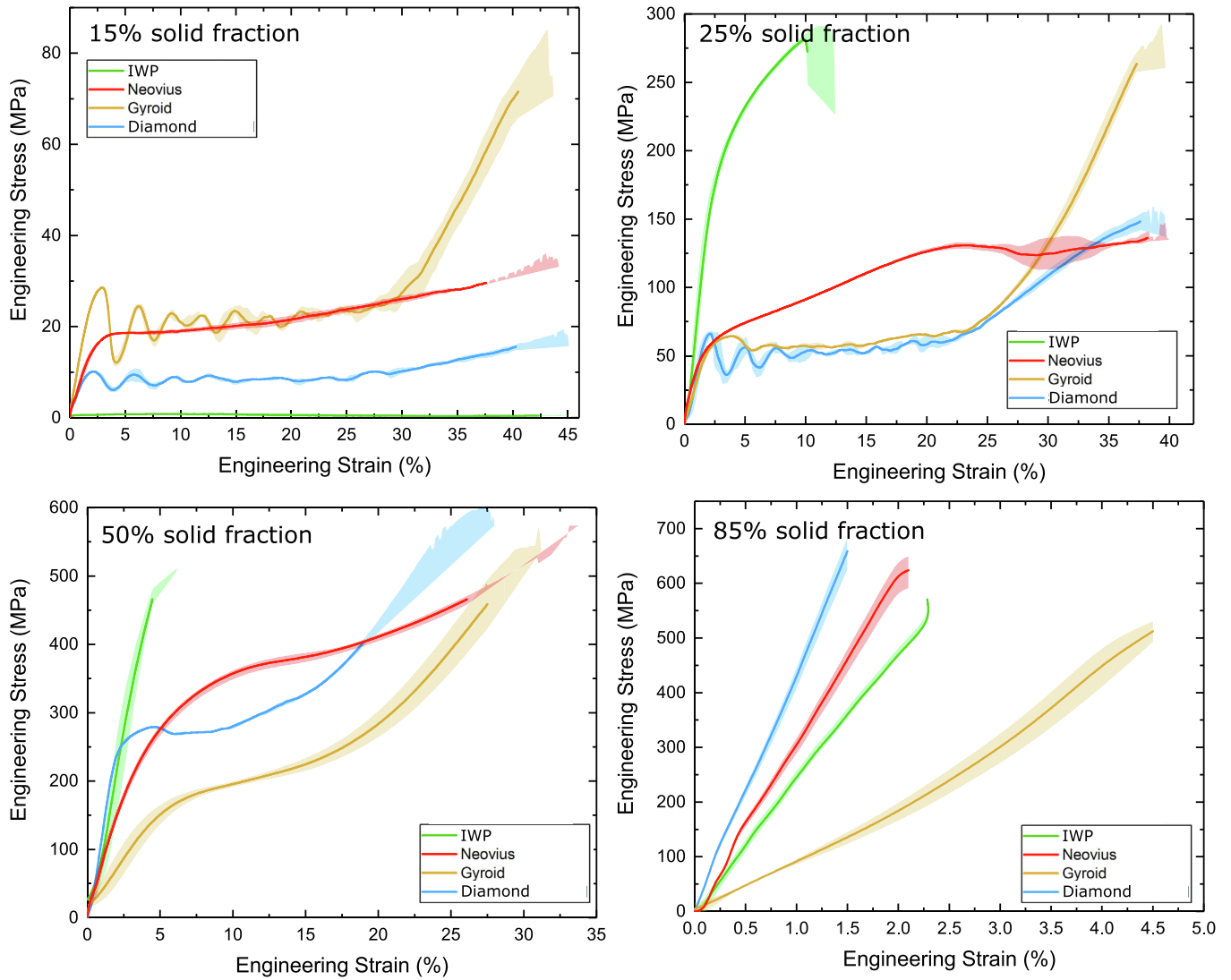


Fig. 11. Mechanical stress-strain curves of the lattices. Solid colour lines indicated the averaged behaviour of 3 repeats and the shaded area the envelope of deviations.

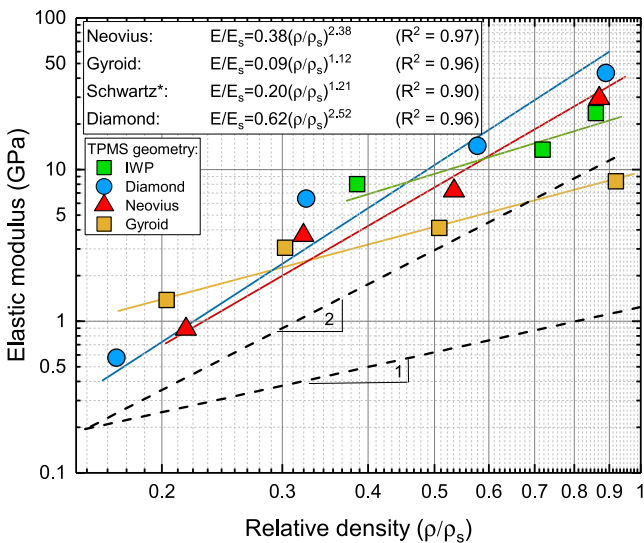


Fig. 12. Elastic modulus vs. relative density Ashby's diagram for the different tested lattices extracted from the data in Fig. 11. Numerical values are presented in Table 4. Experimental data points are fitted by the indicated Ashby-type functions.

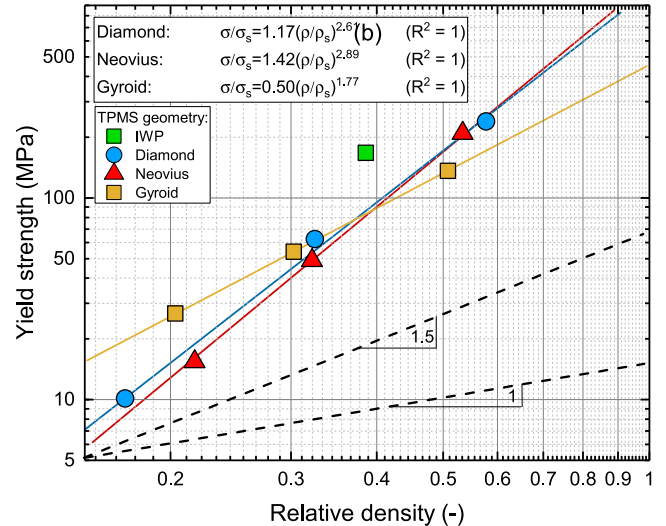


Fig. 13. Yield compressive strength vs. relative density Ashby's diagram for the different tested lattices extracted from the data in Fig. 11. Numerical values are presented in Table 4. Experimental data points are fitted by the indicated the Ashby-type functions.

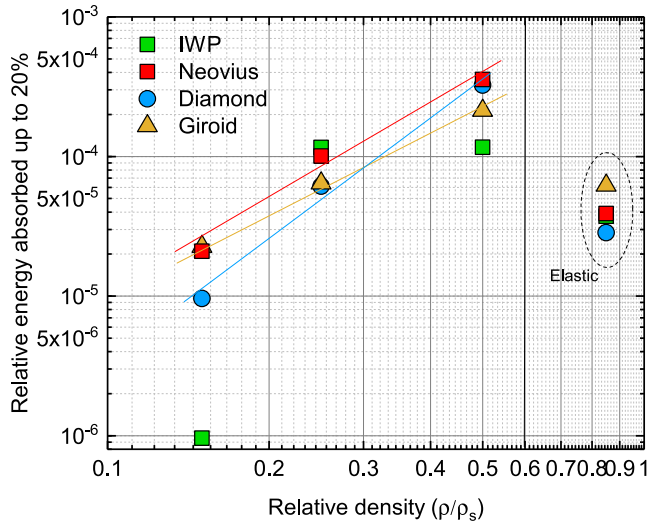


Fig. 14. Energy absorbed up to 20% deformation by the different lattice geometries and solid fractions extracted from the experimental data in Fig. 11.

for the elastic modulus E^* of the lattice and

$$\frac{E^*}{E_s} = C_\sigma \cdot \left(\frac{\rho^*}{\rho_s}\right)^{m_\sigma} \quad (3)$$

for the strength σ^* of the lattice. E_s and σ_s represent the elastic modulus and the yield strength of the solid material (Ti6Al4V in

this case), respectively. C_E , C_σ , m_E and m_σ are lattice constants. The values of m_E and m_σ depend on the deformation mode: for stretch-dominated lattices $m_E = 1$ and $m_\sigma = 1$ and for bend-dominated lattices $m_E = 2$ and $m_\sigma = 1.5$ as indicated in Figs. 12,13. Most of the cellular structures deform in a bend-dominated fashion [39,62].

In terms of stiffness, Diamond and Neovius show bend-dominated behaviour while IWP and Gyroid deformed in a stretch dominated fashion. At lower densities, the performance of the Gyroid lattice is higher than the other three. This situation reverses at higher densities. For fusion medical devices, it is beneficial to reach the desired stiffness while leaving as much space as possible for the bone to grow inside. In terms of strength, Diamond, Neovius, and Gyroid exhibit bend dominated behaviour. The energy dissipated up to 20% strain is presented in Fig. 14. The dissipated energy tends to increase with the solid fraction – for 85% s.f. only 5% strain is considered. It was found that the energy values are quite similar between lattice topologies – except for IWP-15% where the reduced manufacturability impairs the performance.

3.3. Effect of lattice design on the pore size distribution

Following the procedure explained in Section 2.3, maps of the average pore size as a function of the lattice topology, unit cell size, and percentage of porosity were constructed. These are presented in Fig. 15. As observed in the figure, as the solid fraction increases,

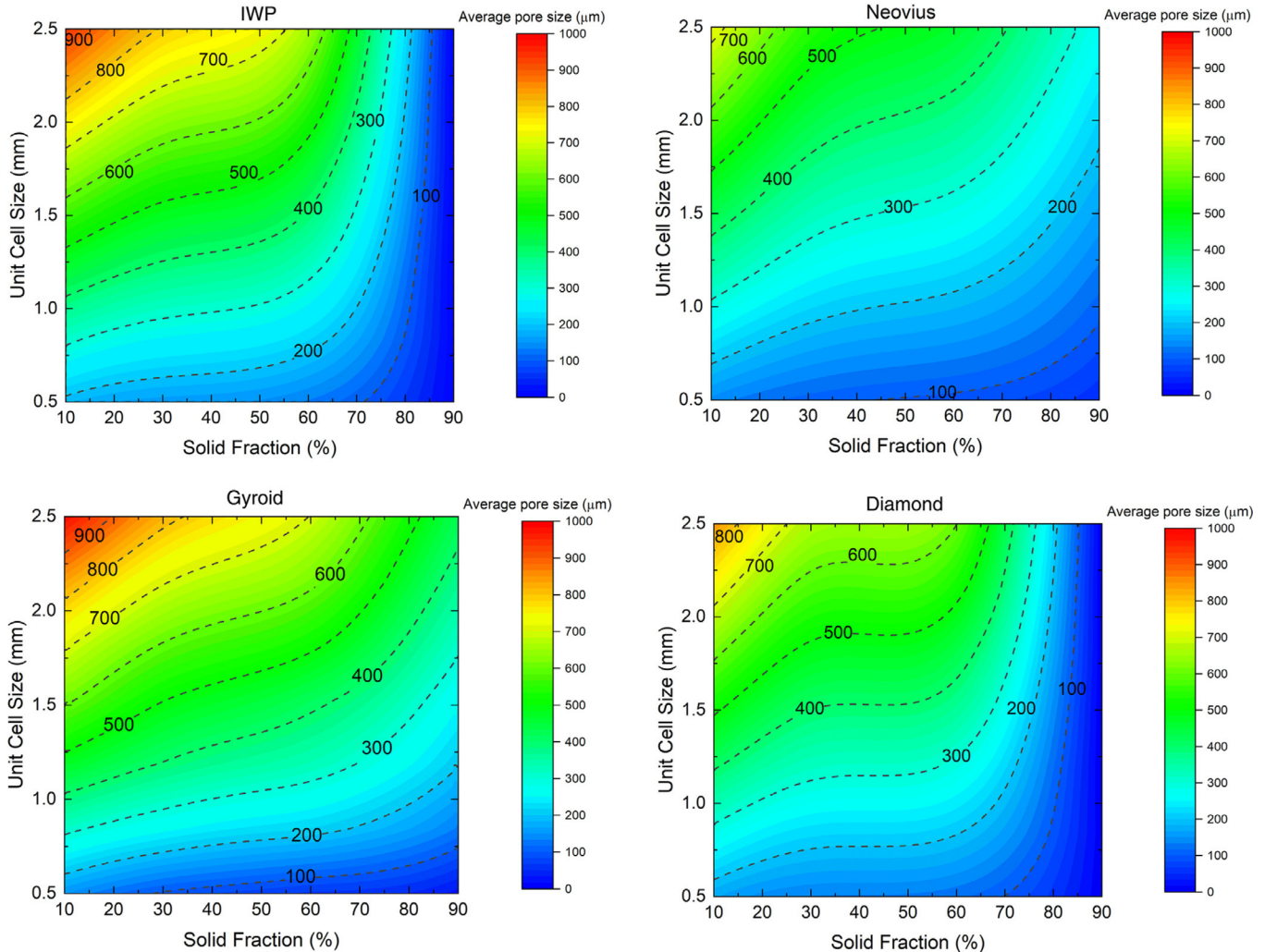


Fig. 15. Calculated maps of pore size as a function of solid fraction and unit cell size for the four geometries under study.

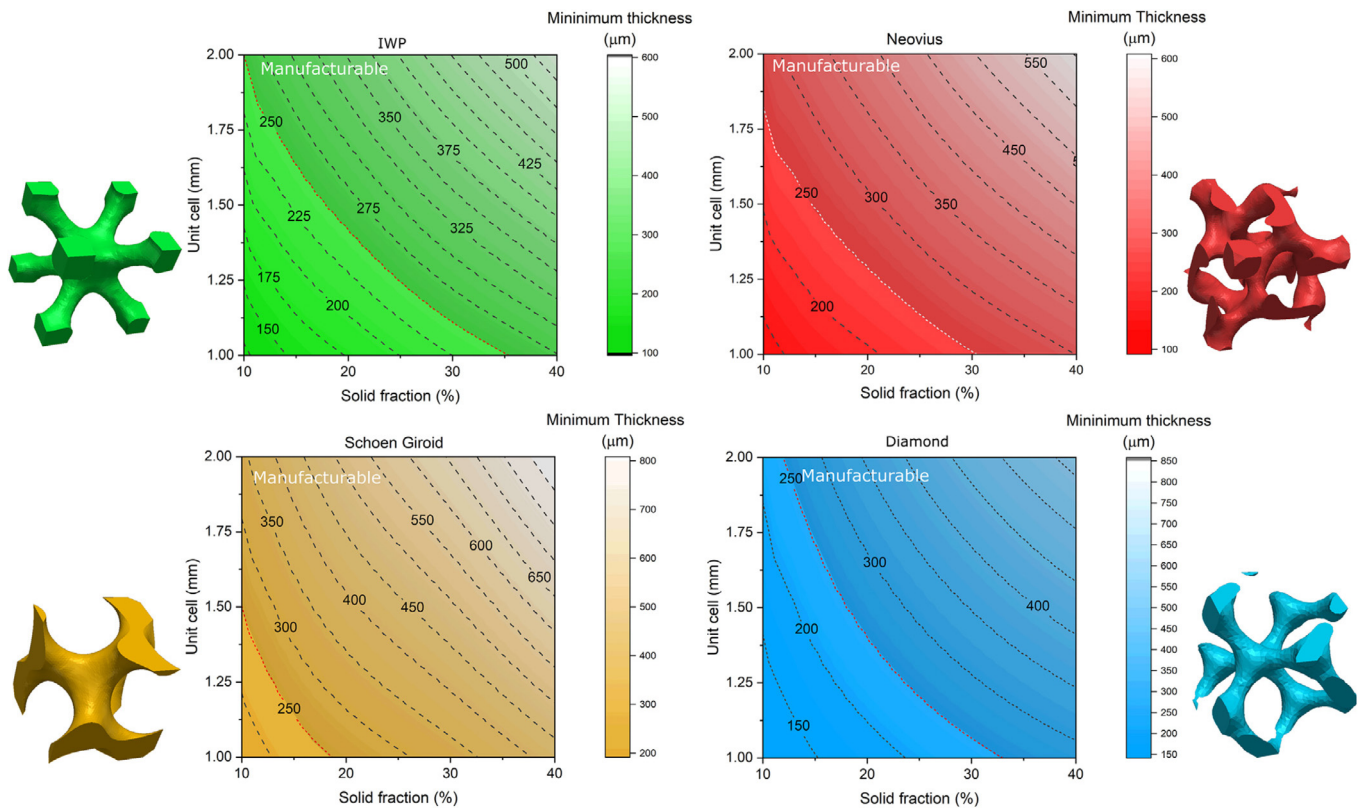


Fig. 16. Minimum thickness for each TPMS as a function of the unit cell and solid fraction. The dashed highlighted border indicates the minimum strut thickness of $250\ \mu\text{m}$ to assure geometrical accuracy based on the experimental observations reported in this work.

the unit cell needs to increase in size to maintain the same average pore size. The unit cell geometry has also a great influence on the average pore size distribution. Schwartz W and Giroid present higher average pore size for the same range solid fraction and unit cell size. These maps are later used in the discussion section to study the position of the preferred pore size range for the four type of lattices.

4. Discussion

4.1. Manufacturability design maps

With the results presented in Section 2.1, we constructed manufacturing design maps. The minimum feature thickness of each geometry is chosen as a variable which controls the manufacturability of the lattice. A value of $250\ \mu\text{m}$ is assumed as the minimum printable thickness with an admissible accuracy on the basis of the results presented above. This is $50\ \mu\text{m}$ higher from what proposed in [39]. However, the value presented in that study was theoretical and it was not supported by experimental data. The minimum feature thickness for lattices with unit cells between 1 and 2 mm and solid fractions between 10 and 40% are computed in Fig. 16. These porosities are the most relevant for implant applications – this will be explained in Section 3.2. The values for the unit-cells are chosen as optimal for osseointegration – this will be explained in Section 3.3. The manufacturability criterion showed that IWP and Diamond present the narrowest manufacturable regions – those geometries result impossible to manufacture at high porosities and small unit cells. This is in agreement with our experimental analysis. These maps will be used later in the design process presented in Section 4.4.

4.2. Tailoring the mechanical behaviour of the lattice

In the following sections the results obtained in Section 3.2 are used to study the effect of the material selection on the lattice behavior and the influence of porosity and geometry on the lattice anisotropy.

4.2.1. Material selection for biomedical lattices

On the basis of the results presented in Section 3.2, the effect of material selection on the effective stiffness of the lattices is discussed. Eqs. (2) and (3) are used to extrapolate the behaviour of the topologies to other bio-medical materials. Results are presented in Fig. 17. The effective modulus of each lattice is presented as a function of its relative density and material used. Trabecular and cortical bone has a wide range of mechanical properties as indicated in Table 3. The regions with values matching approximately the stiffness of spinal cortical (18–28 GPa) and trabecular bone (0.1–1 GPa) are indicated with white dashed lines – trabecular bone has lower stiffness than cortical bone. As expected, low stiffness materials such as PEEK or β -Ti alloys allows one to manufacture higher relative densities. On the other hand, the type of topology also has an important effect on the position of these optimal regions for stiffness matching. Neovius and Diamond present the stiffness matching at higher solid fractions than Gyroid or IWP topologies – higher solid fractions are generally easier to manufacture as they present thicker features. It is important to notice that these results are approximated and they might differ as a function of the particular manufacturability of each one of the materials here considered and the type of bone under consideration. In any case, the results presented here can be used for initial design purposes and should provide a useful guideline. It is important to note that, in the case of Ti-6Al-4V, targeting trabecular bone (solid

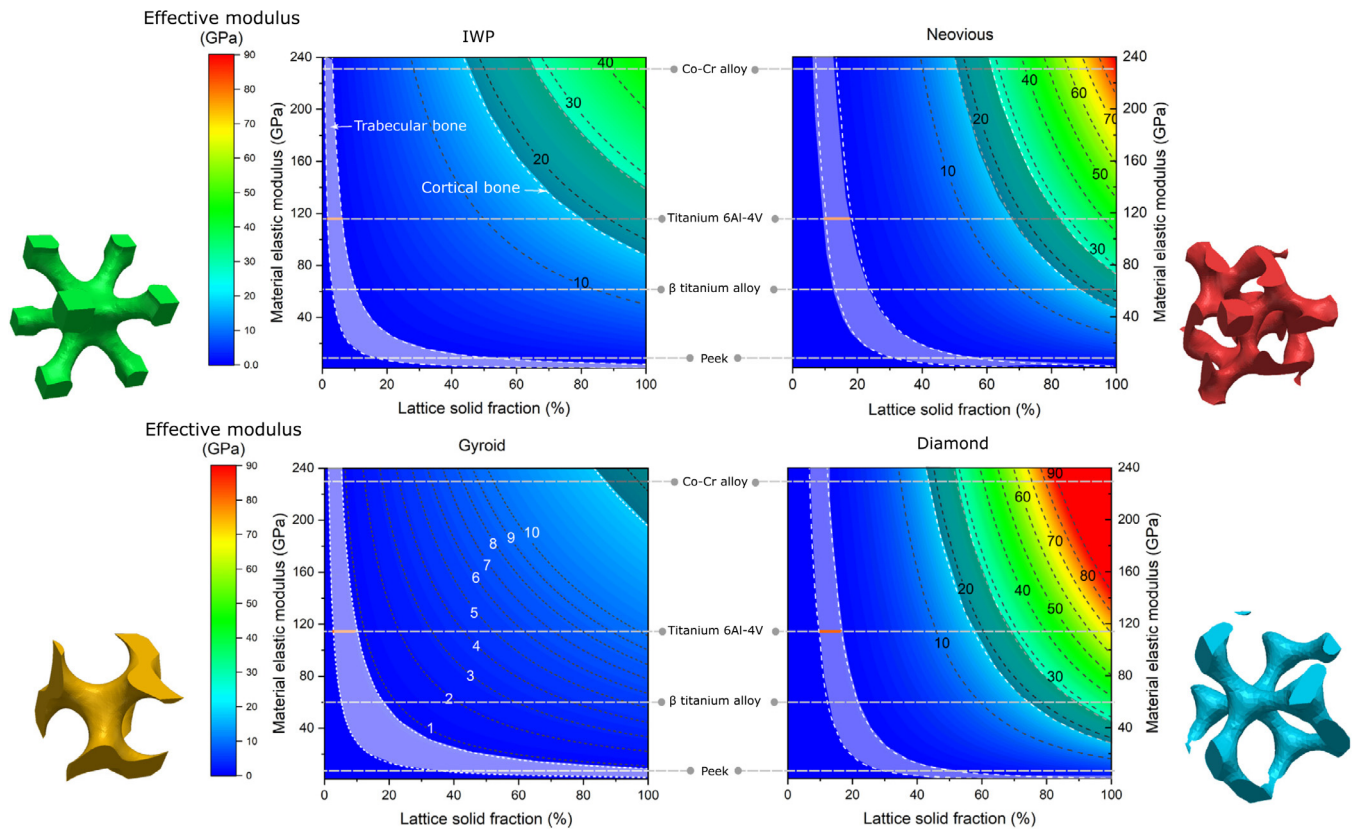


Fig. 17. Effective elastic modulus maps for each of the lattice geometries as a function of its solid fraction and the material used to build the lattice. Four reference materials are indicated as horizontal dashed lines: Co-Cr alloy, Ti 6Al4V, β -Ti, and PEEK.

Table 3

Mechanical properties of different trabecular and cortical bone tissue extracted from Li et al. [63]

Type of tissue	Ultimate strength (MPa)	Elastic modulus (GPa)
<i>Cortical Bone</i>		
Tibia osteons (longitudinal)	–	22.5
Tibia interstitial lamellae (longitudinal)	–	25.8
Femur	194	17.6
Tibia	195	28.0
<i>Trabecular Bone</i>		
Lumbar vertebra (male)	4.60	0.06
Lumbar vertebra (female)	2.70	0.04
Tibia head (male)	3.90	0.03
Tibia head (female)	2.20	0.02
Tibia	8.80	0.64
Vertebra (vertical)	2.5	0.07
Vertebra (horizontal)	0.9	0.02
Proximal tibia	5.33	0.45
Femur	7.36	0.39
Lumbar spine	2.45	0.07
Lumbar spine	1.55	0.02

fraction below 15–20%) the yield stress observed in Fig. 14 is lower than those of trabecular bone [63–65]. This emphasises the need of a new range of alloys with larger strength/stiffness ratios

4.2.2. Anisotropic behaviour of the lattices

Another important consideration in the design of metal structures as bone substitute is the anisotropic behaviour of the lattices. An anisotropy mismatch may lead to stress-shielding. Tra-

becular and cortical bone can have different anisotropic properties depending on the anatomical location. For the focus in this study (vertebral spinal fusion), trabecular bone in the vertebral is fairly isotropic while cortical bone on the surface can have a strong anisotropy, usually aligned along the local loading direction [66,67].

With this in mind, the anisotropy – or lack thereof – of each of the lattices was computed via finite element analysis (FEA) following the procedure described by Xu et al. [44]. FEA models of the 16 different lattices were constructed and deformed under 6 different loading conditions (3 pure tension cases and 3 pure shear cases). With the forces obtained from these 6 cases, the 21 unknown constants of the fourth order stiffness matrix \mathbf{C} can be identified. As an example, for a loading case of pure compression along the X direction:

$$\begin{bmatrix} \varepsilon_{11} \\ \varepsilon_{22} \\ \varepsilon_{33} \\ \varepsilon_{12} \\ \varepsilon_{23} \\ \varepsilon_{13} \end{bmatrix} = \begin{bmatrix} \Delta \\ 0 \\ 0 \\ 0 \\ 0 \\ 0 \end{bmatrix} \rightarrow \begin{bmatrix} \sigma_{11} \\ \sigma_{22} \\ \sigma_{33} \\ \sigma_{12} \\ \sigma_{23} \\ \sigma_{13} \end{bmatrix} = \begin{bmatrix} C_{11}/\Delta \\ C_{22}/\Delta \\ C_{33}/\Delta \\ C_{12}/\Delta \\ C_{23}/\Delta \\ C_{13}/\Delta \end{bmatrix} \quad (4)$$

where Δ is the displacement imposed in the boundary.

The computed stiffness matrix is then used to calculate the elastic modulus of the lattice in any direction within the 3D space. The 3D stiffness surfaces for the four different geometries are presented in Fig. 18-left for 15% solid fractions. The more spheric the surface, the more isotropic the lattice is. For comparison, an example 3D stiffness surface of trabecular bone (constructed from

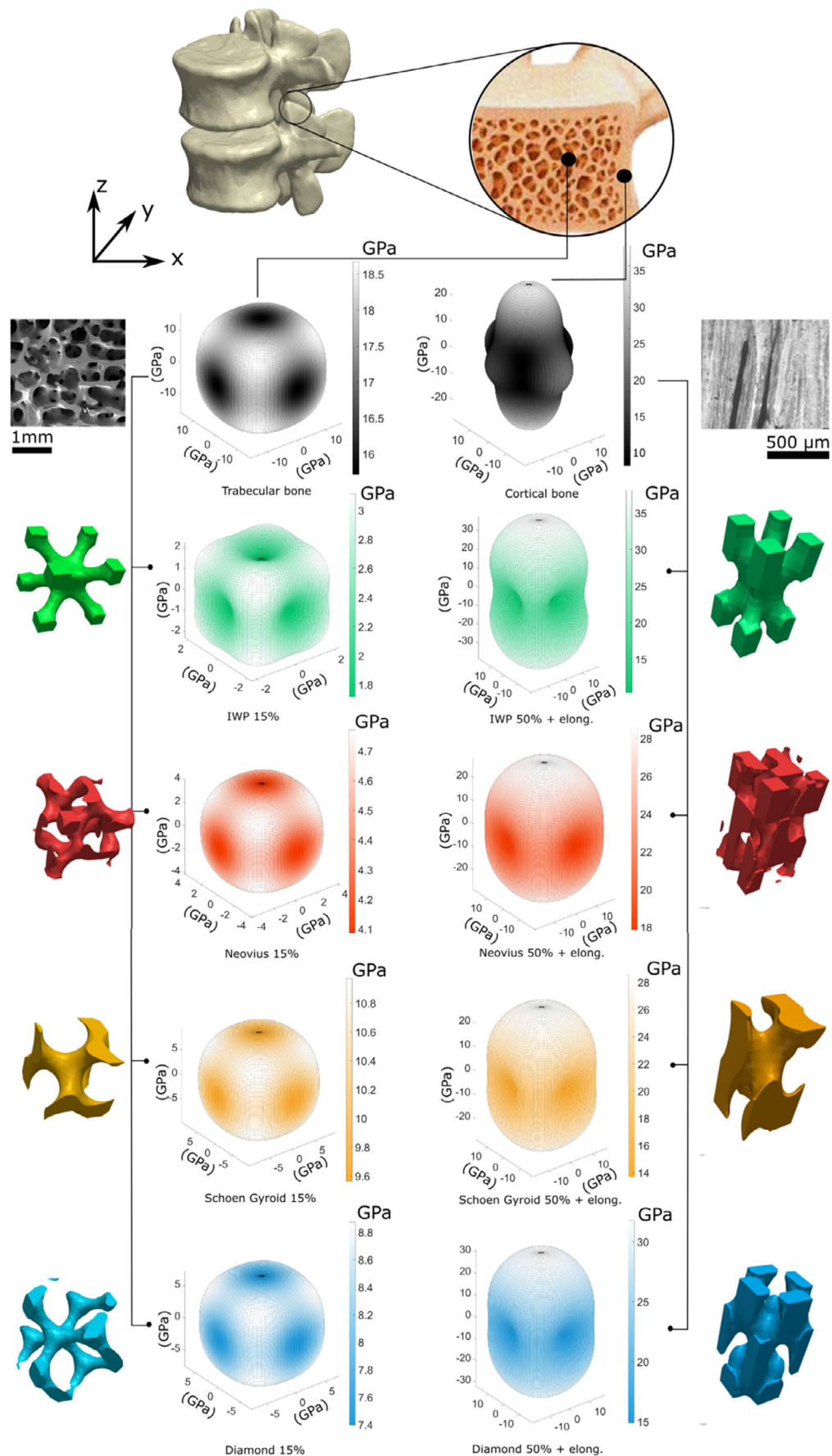


Fig. 18. (Left) 3D bulk elasticity surfaces of the different lattice geometries under study along with the elastic surface for trabecular bone [66] in black. (Right) 3D bulk elasticity surfaces for modified lattices with a 100% elongation along the Z direction and elastic surface for cortical bone [66] in black.

literature data [66]) is also shown. It is important to note that natural bone values are dependent on the type of bone, age or gender [66,68–70], but the qualitative comparison between lattices and bone is still relevant. Results show that IWP has the highest anisotropy. It has lower stiffness along axial directions than longitudinal directions. This is explained by the beam arrangement of the lattice. The other topologies exhibit a more isotropic response, much closer to that of body vertebrae trabecular bone. This is an important design consideration.

On the other hand, there might be medical applications where the loading conditions require of anisotropic structural properties to mimic the replaced bone, i.e. long bone reconstructions. Cortical anisotropic stiffness cannot be replicated with standard lattices (see Fig. 18-right where anisotropic cortical bone properties have been used as an example). However, geometrical dilation of the lattice topology in one direction allows one to tailor anisotropy. Applying a 100% dilation along the Z direction with 50% porosity – to roughly target cortical bone stiffness – allows one to achieve 3D elastic surfaces which mimic the behaviour of cortical bone.

The influence of porosity on the anisotropy of the lattice is critical. It is desirable to have topologies where porosity has little influence on anisotropy – this leaves porosity as a free parameter to tailor the stiffness of the implant. The effect of porosity on anisotropy for the different topologies is shown in Fig. 19. Two different trends are observed: lattices with strong porosity effect on the anisotropy (IWP) and lattices with little influence (Diamond, Neovius, and Gyroid) – the latter is more desirable for implant design. In summary, by choosing the correct topology and applying geometrical dilation, the specific anisotropic properties of the different bone types can be achieved artificially. Moreover, the porosity of the lattice can be chosen as a free parameter (except for IWP) to tailor the stiffness of the matrix to both cortical and trabecular bone.

4.3. Predicted effect of lattice design on osseointegration

The osseointegration capability of each lattice geometry has been observed to be affected by the pore size and curvature of the geometry [71,18,72,39,46]. The review of Tan et al. [39] summarises the effect of the mean pore size on bone ingrowth. Two

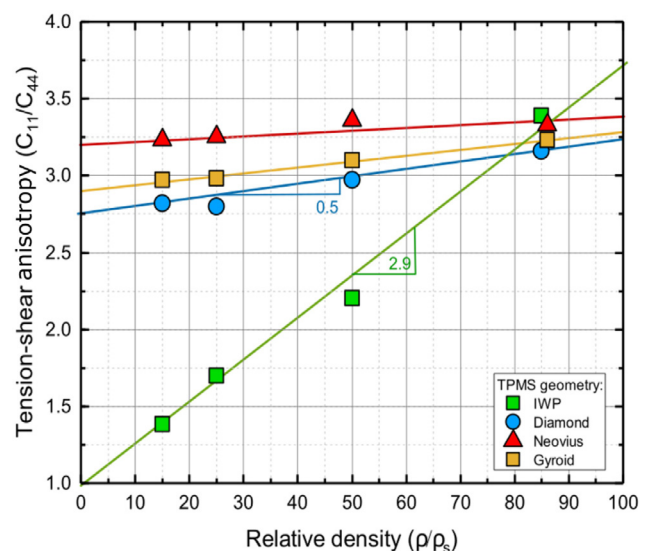


Fig. 19. Effect of the solid fraction on the tension/shear anisotropy factor (C_{11}/C_{44}) obtained from numerical simulations for the different lattice geometries.

main critical biological processes are affected by the pore size: (1) the initial osteoblast cell colonisation and (2) the following vascularisation of the pre-bone tissue [46]. The former has been found to be promoted by smaller pore sizes (faster colonisation when pores are $< 600 \mu\text{m}$ [39,47,46,45], the latter requires large pores to embed the blood vessels ($> 300 \mu\text{m}$) [50–53]. These two regimes are illustrated conceptually in Fig. 20. These approximated regions are based on several literature studies on pore size influence on osseointegration and actual ranges used in commercial latticed implants [71,72,39,46,47,45,50–53]. Conceptually, the combination of these requirements is satisfied in an approximated pore size range of $300 \mu\text{m} < \text{pore} < 600 \mu\text{m}$ [39]. This is the range used in this study as the preferred pore size. It is important to note that these represent soft limits of the preferred pore sizes and are approximations based on the literature data. Although not a biological aspect, another reason to avoid small pore sizes is sintering of

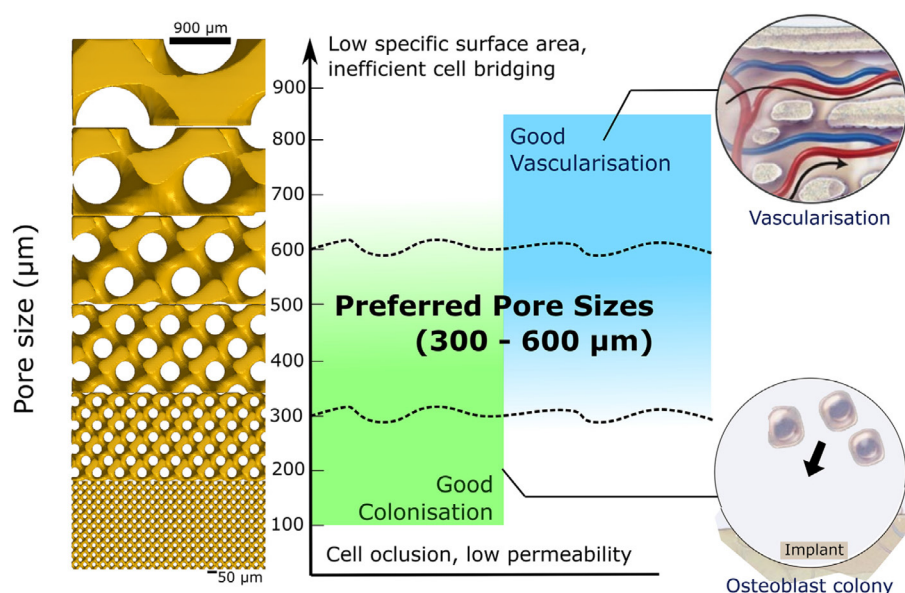


Fig. 20. Diagram of the approximated preferred pore sizes for both bone stages: bone colonisation and bone vascularization. The tendencies are conceptual and extracted from studies in the literature [71,72,39,46,47,45,50–53]. The approximated preferred region for both processes together based on the literature studies [71,72,39,46,47,45,50–53] extends roughly from $300 \mu\text{m} < \text{pore} < 600 \mu\text{m}$.

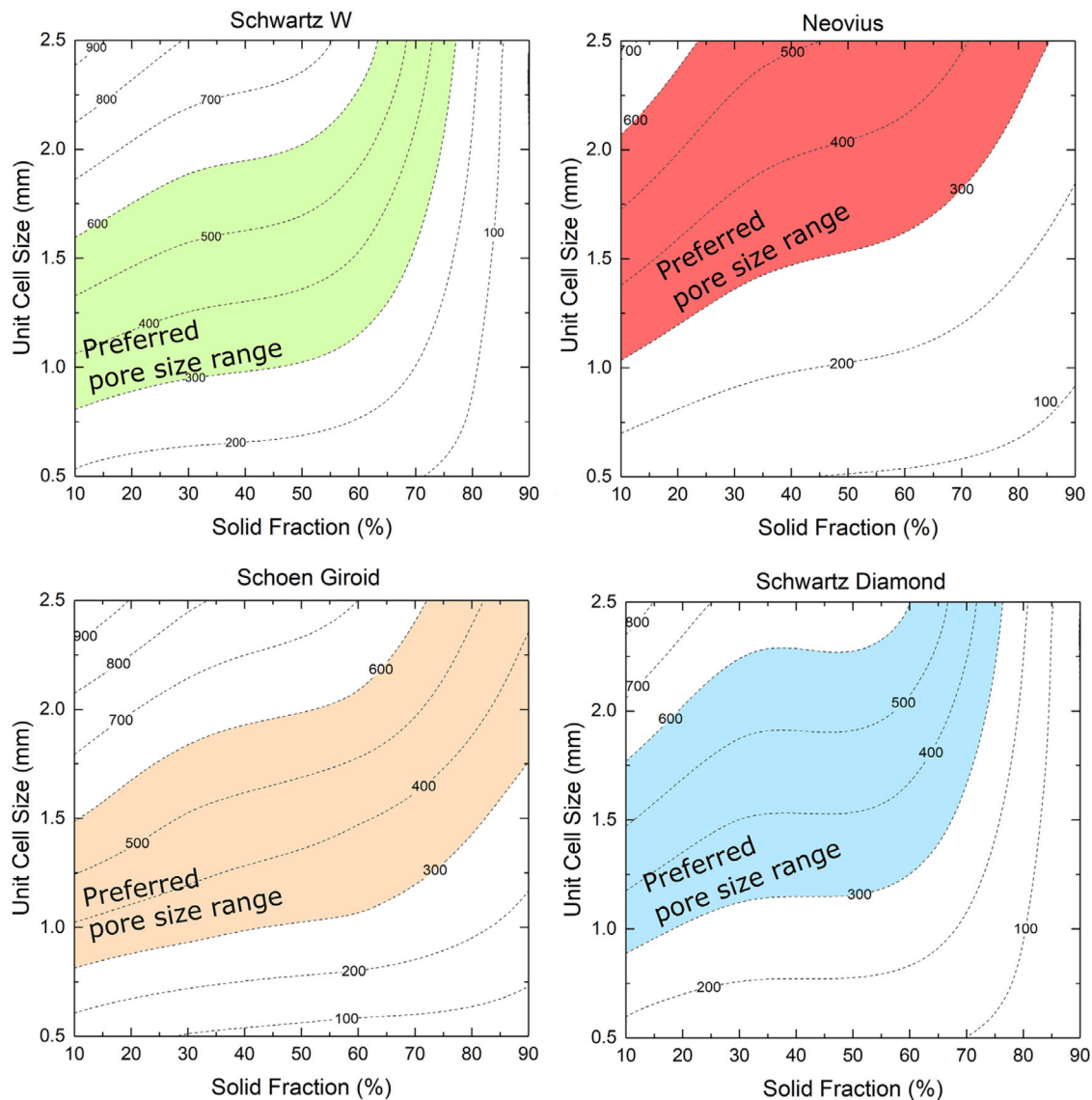


Fig. 21. Calculated conceptual preferred pore size region for each lattice type approximated based on the literature of osseointegration studies [71,72,39,46,47,45,50–53].

powder during the additive process. This causes powder trapping and pore occlusion. This phenomenon is observed for pore sizes of 300 μm and below. The preferred pore size region is marked for the four type of lattices in Fig. 21. The lattice topology has a great influence on the size and location of this preferred band. For example, Neovius presents the preferred band at larger unit cell sizes than IWP and Gyroid. This aspect, combined with the other design constraints described previously (manufacturability and mechanics), will make some geometries undesirable for porous implants. This is discussed further in Section 4.4.

On the other hand, the macroscopic surface curvature has been observed to play an important role on the initial cell attachment [18,31]. The avoidance of sharp edges and geometries with close-to-zero curvatures have been hypothesized to enhance the cell attachment [18,31], although it is still a controversial topic. This macroscopic geometry is different to the microscopic roughness (not treated in this study) which has been observed to have a beneficial effect on cell adhesion and proliferation [73–75]. Focusing on the macroscopic surface curvature and based on this criterion [18,31], TPMS are believed to be good candidates for osseointegrative structures due to its zero-curvature property. TPMS-skeleton lattices with 50% porosity maintain this desirable prop-

erty. However, as the solid fraction decreases – or increases – the curvature deviates from zero. The driving force for decreasing the lattice solid fraction is the desire to match stiffness. Therefore, the deviation from the zero-curvature property is imposed by material choice (for Ti-6Al-4V, the preferred porosity sits around 15–25%). Using lower stiffness materials will allow one to increase the lattice solid fraction to those with closer-to-zero curvatures.

4.4. Isolating an optimal design space and application to spinal implants

The individual models and methods described previously are now combined to into a unified design framework, with specific emphasis on interbody spine fusion devices. This considers manufacturability, mechanical behaviour and osseointegration. The goal is to achieve a global optimised lattice. This concept is presented in Fig. 22. The framework is as follows: for each lattice geometry, the design space – in terms of porosity and unit cell size – is reduced by the requirements of (1) stiffness range matching of vertebrae bone, (2) minimum printable thickness, and (3) optimal pore size for bone ingrowth. The frontiers drawn by those requirements enclose the optimal design area.

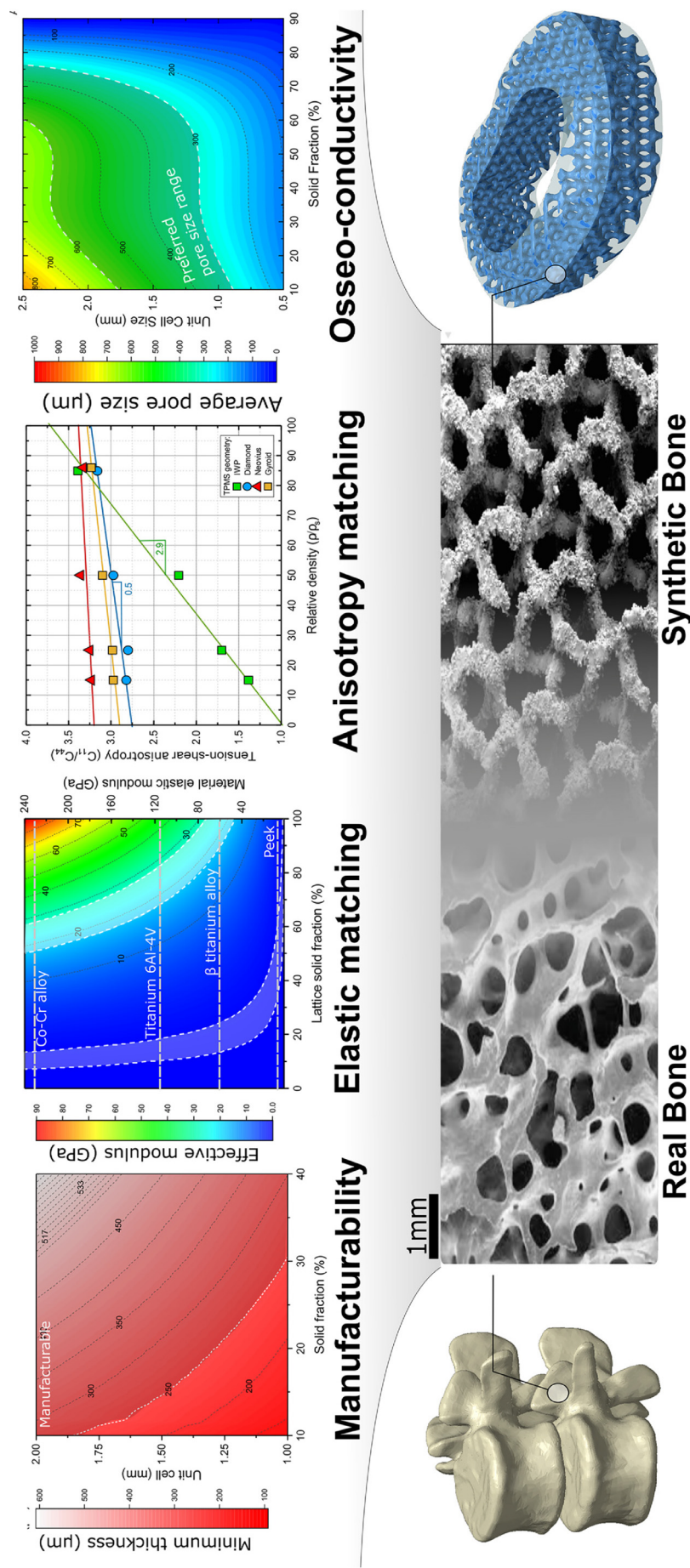


Fig. 22. Diagram of the unified design framework proposed in this work. The combined properties of manufacturability, mechanical behaviour, and osseo-integration of the implant are simultaneously matched to the properties of bone.

Fig. 22. Diagram of the unified design framework proposed in this work. The combined properties of manufacturability, mechanical behaviour, and osseo-integration of the implant are simultaneously matched to the properties of bone.

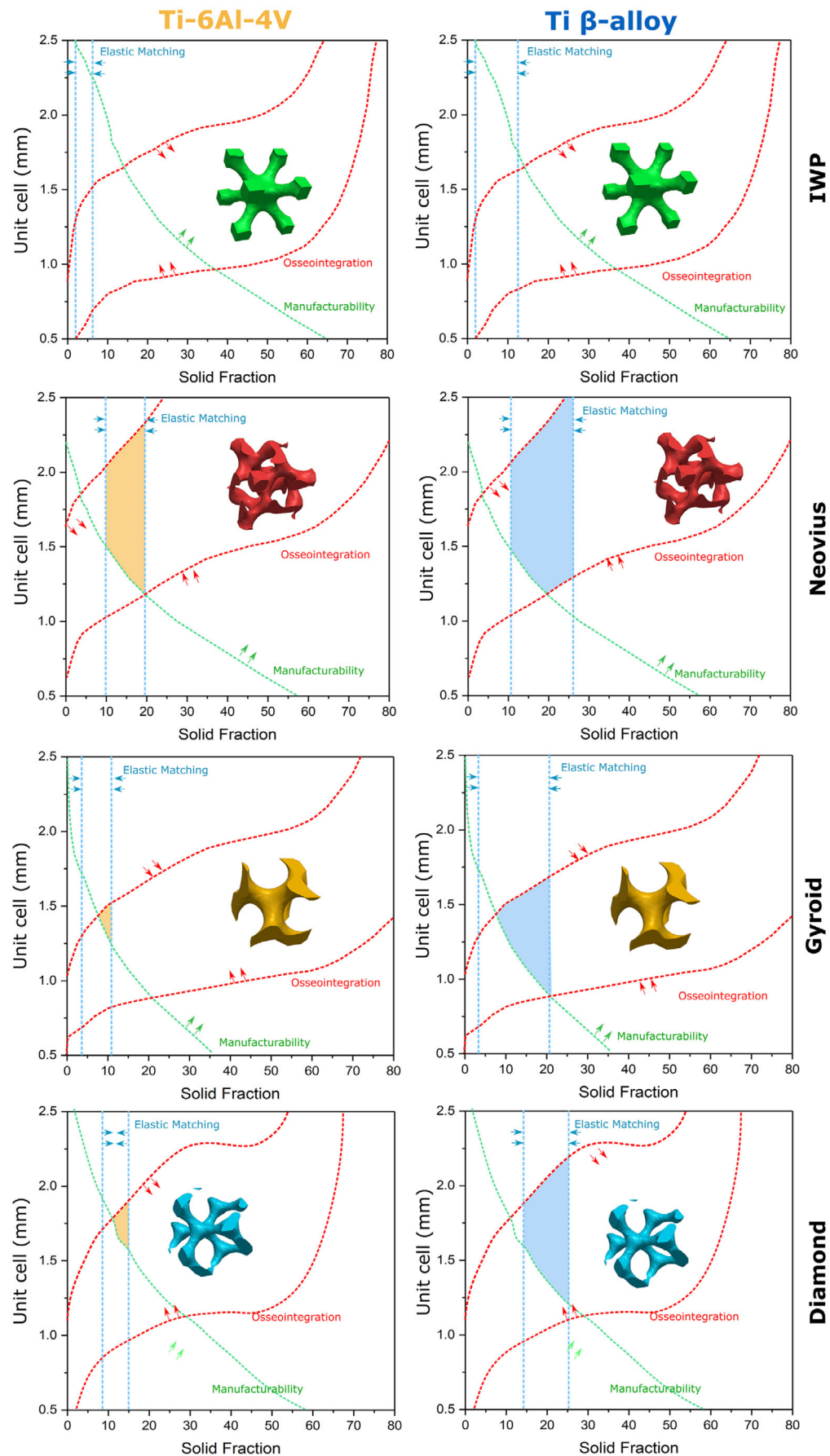


Fig. 23. Lattice design regions obtained by following the procedure in Fig. 22. In the left hand side column maps, Ti-6Al-4V is used as substrate material. On the right hand side maps, a β -type titanium alloy is assumed [80].

Table 4

Mechanical properties measured experimentally of the different lattice geometries and porosities along with the statistical deviations

Geometry	Ideal Porosity (%)	Elastic modulus (GPa)	Yield stress (MPa)	Maximum stress (MPa)	Plateau stress (MPa)	Crushing	Fracture
IWP	15	–	–	0.8 ± 0.03	–	No	Densification
	25	8 ± 0.4	167 ± 2	282 ± 5	–	No	Brittle Fracture
	50	13.5 ± 2.6	–	–	–	–	No fracture
	85	23.6 ± 1.4	–	–	–	–	Elastic Loaded
Neovius	15	0.9 ± 0.05	15.4 ± 0.6	18.85 ± 0.3	20.0 ± 1	No	Densification
	25	3.7 ± 0.2	48.8 ± 0.8	22 ± 1.1	–	No	Densification
	50	7.2 ± 0.6	209 ± 4	369 ± 5.2	–	–	Densification
	85	29.5 ± 3.2	–	–	–	–	Elastic Loaded
Schoen Gyroid	15	1.3 ± 0.02	26.7 ± 0.1	29 ± 0.4	20.9 ± 0.8	Yes	Densification
	25	3 ± 0.2	54 ± 0.7	65 ± 2.2	60.1 ± 0.9	Yes	Densification
	50	4.1 ± 1.3	136 ± 14	182 ± 14.2	–	No	Densification
	85	8.4 ± 1.8	–	–	–	–	Elastic Loaded
Diamond	15	0.5 ± 0.02	10.11 ± 0.2	10 ± 0.1	8.7 ± 0.4	Yes	Densification
	25	6.4 ± 0.6	62.37 ± 6	66 ± 5.3	51.7 ± 3	Yes	Densification
	50	14.3 ± 0.3	239 ± 0.8	279 ± 1.2	272 ± 1	Yes	Densification
	85	43.3 ± 2	–	–	–	–	Elastic Loaded

This design framework has been applied to the four geometries treated in this paper. Optimal design spaces are presented in Fig. 23. Left hand side assumes that Ti-6Al-4V alloy has been used for manufacturing. A strong dependency of the optimal design region (both size and localisation) with lattice geometry is observed. Ranked from better to worst in terms of the design area: (1) Neovius, (2) Diamond and Gyroid, and (3) IWP. The latter one lacks a space that fulfills all the stated requirements. Thus, the Neovius topology presents the choice for porous medical devices. Combining good specifications in each of the three indexes is critical: e.g. Diamond and Neovius topologies present similar levels of stiffness, but the reduced manufacturability of the Diamond topology forces the use of larger cell sizes and porosities, therefore making it less adequate for implantation.

To highlight the importance of material selection on the design space, a second design space is computed – see right hand side of Fig. 23. In this case, a β titanium alloy with 50% the elastic modulus of Ti-6Al-4V is assumed. These type of alloys have been proved to being able to lower its elastic modulus, keeping reasonable strengths and being able to be manufactured by SLM processes [76–78]. The effect of the material on the design space is clear: lower stiffness materials increase the design space – a larger number of optimal porosities and unit cells can be achieved. Moreover, the new optimal regions extend away from the manufacturability limit (higher solid fractions and larger unit cells), thus improving the quality of the manufactured lattice and therefore the performance of the implant. This exercise reinforces the need for novel bio-compatible materials with lower elastic modulus. Novel materials and the advanced manufacturing of biomedical lattices will allow engineers to design medical devices with improved bio-mechanical performance when compared to the current grades of implants.

5. Summary and conclusions

The role of lattice topology (Schwarz Diamond, Schwarz IWP, Neovius and Schoend Gyroid) and solid fraction (15, 25, 50, 85%) on the properties of porous titanium for implant applications have been studied using a combination of experimental and computational approaches. The following specific conclusions can be drawn from this work:

1. It has been observed – by a comparative accuracy analysis on computed microtomography results – that the choice of lattice topology has a strong influence on the geometrical precision

which can be achieved. Schwarz IWP and Schwarz Diamond present significantly worse accuracy than Gyroid and Neovius. For the state-of-the-art 3D technology used here, a minimum strut thickness of 250 μm is necessary to achieve acceptable geometrical accuracy.

2. A direct correlation between manufacturability and mechanical properties is proven. The poor manufacturability of the IWP topology results in lower mechanical properties and behaviour. This makes IWP unsuitable for the purpose of the study. Moreover, the results confirm a capacity to tune porous structures to match the elastic requirements of natural bone.
3. Optimal lattice design must be accompanied of appropriate material selection. Lower stiffness materials (e.g. β -titanium alloys and PEEK) allow to relax the manufacturability limitations and enlarge the design regions where lower stiffness can be achieved.
4. The conceptual lattice design requirements which are likely to be needed for osseo-integration – critical pore sizes for both cell growth and vascularisation – have been identified. This is based on a preferred pore size of 300 μm < pore < 600 μm . A combination of lattice geometry, optimal unit cell size, and desired porosities determine design spaces, in particular making some of the lattices not suitable for implantation. Both IWP and Neovius topologies offer suitable osseo-integration regions at larger unit cells – with the consequent improvement in the quality of the printed structures.
5. The models and design requirements for the three main aspects studied – manufacturability, mechanical behaviour and osseo-integration – have been combined in a unified conceptual design framework. This is used to define optimal design regions for the different topologies. These are ranked based on our requirements for Ti-6Al-4V as follows: Neovius presents the largest design flexibility, Gyroid and Diamond have slightly smaller design areas and IWP lacks an optimal design space. For lower stiffness materials such as β -titanium alloys, the design area is increased for all topologies.

6. Statistical analysis

Statistical errors were considered in this study, especially in the measurement of the mechanical properties and manufacturing errors of the different lattices. For this purpose, three repeats were carried out. The mechanical response was then averaged. Good repeatability was found in all the tests. The shaded area in Fig.

11 represents the maximum and minimum stress-strain curve extracted from the 3 repetitions. The solid line indicates the average response – using the arithmetic mean. These values are used later in the design analysis. The statistical deviation for each of the measured mechanical properties are included in Table 4. These correspond to the range of the mechanical properties measured from the 3 repetitions. In the case of the solid fraction, three different manufactured lattices were weighted and analysed. The arithmetic averaged solid fraction is presented in Fig. 5.

Data availability

For access to the raw data related to this article please contact the corresponding author.

References

- [1] D. Lopes, C. Martins-Cruz, M.B. Oliveira, J.F. Mano, Bone physiology as inspiration for tissue regenerative therapies, *Biomaterials* 185 (2018) 240–275.
- [2] M.A.K. Liebschner, M.A. Wettergreen, Topics in Tissue Engineering 2003. Chapter 6: Optimization of Bone Scaffold Engineering for Load Bearing Applications, University of Oulu, 2003.
- [3] J.G. Wells, R.D. Rawlings, Acoustic emission and mechanical properties of trabecular bone, *Biomaterials* 6 (1985) 218–224.
- [4] P. Augat, S. Schorlemmer, The role of cortical bone and its microstructure in bone strength, *Age Ageing* 35 (2006) ii27–ii31.
- [5] G. Osterhoff, E.F. Morgan, S.J. Shefelbine, L. Karim, L.M. McNamara, P. Augat, Bone mechanical properties and changes with osteoporosis, *Injury* 47 (2016) S11–S20.
- [6] R. Oftadeh, M. Perez-Viloria, J.C. Villa-Camacho, A. Vaziri, A. Nazarian, Biomechanics and mechanobiology of trabecular bone: a review, *J. Biomech. Eng.* 137 (2015) 010802.
- [7] F. Marinuzzi, F. Bini, A. Marinuzzi, F. Zuppante, A. De Paolis, R. Pecci, R. Bedini, Technique for bone volume measurement from human femur head samples by classification of micro-CT image histograms, *Annali dell'Istituto superiore di sanità* 49 (2013) 300–305.
- [8] F. Marinuzzi, A. Marinuzzi, F. Bini, F. Zuppante, R. Pecci, R. Bedini, Variability of morphometric parameters of human trabecular tissue from coxo-arthritis and osteoporotic samples, *Annali dell'Istituto superiore di sanità* 48 (2012) 19–25.
- [9] F.S.L. Bobbert, A.A. Zadpoor, Effects of bone substitute architecture and surface properties on cell response, angiogenesis, and structure of new bone, *J. Mater. Chem. B* 5 (2017) 6175–6192.
- [10] N. Reznikov, O.R. Boughton, S. Ghouse, A.E. Weston, L. Collinson, G.W. Blunn, J.R. Jeffers, J.P. Cobb, M.M. Stevens, Individual response variations in scaffold-guided bone regeneration are determined by independent strain- and injury-induced mechanisms, *Biomaterials* 194 (2019) 183–194.
- [11] Y. Yan, H. Chen, H. Zhang, C. Guo, K. Yang, K. Chen, R. Cheng, N. Qian, N. Sandler, Y.S. Zhang, H. Shen, J. Qi, W. Cui, L. Deng, Vascularized 3D printed scaffolds for promoting bone regeneration, *Biomaterials* 190–191 (2019) 97–110.
- [12] T.A. Decoster, R.J. Gehlert, E.A. Mikola, M.A. Pirela-Cruz, Management of Post-traumatic Segmental Bone Defects, Technical Report, 2004. URL: <https://insights.ovid.com/pubmed?pmid=14753795>.
- [13] N. Attias, R.E. Lehman, L.S. Bodell, R.W. Lindsey, Surgical Management of a Long Segmental Defect of the Humerus Using a Cylindrical Titanium Mesh Cage and Plates A Case Report, Technical Report, 2005. URL: <https://insights.ovid.com/pubmed?pmid=15758677>.
- [14] M.S. Sørensen, K.G. Gregersen, T. Grum-Schwensen, D. Hovgaard, M.M. Petersen, Patient and implant survival following joint replacement because of metastatic bone disease, *Acta Orthopaedica* 84 (2013) 301–306.
- [15] M. Niinomi, Recent metallic materials for biomedical applications, *Metall. Mater. Trans. A* 33 (2002) 477–486.
- [16] K. Alvarez, H. Nakajima, Metallic scaffolds for bone regeneration, *Materials* 2 (2009) 790–832.
- [17] T. Karachalios, C. Tsatsaronis, G. Efrimidis, P. Papadellis, G. Lyritis, G. Diakomopoulos, The long-term clinical relevance of calcar atrophy caused by stress shielding in total hip arthroplasty: a 10-year, prospective, randomized study, *J. Arthroplasty* 19 (2004) 469–475.
- [18] A.A. Zadpoor, Bone tissue regeneration: the role of scaffold geometry, *Biomater. Sci.* 3 (2015) 231–245.
- [19] S.-W. Yook, H.-E. Kim, Y.-H. Koh, Fabrication of porous titanium scaffolds with high compressive strength using camphene-based freeze casting, *Mater. Lett.* 63 (2009) 1502–1504.
- [20] J.P. Li, P. Habibovic, M. van den Doel, C.E. Wilson, J.R. de Wijn, C.A. van Blitterswijk, K. de Groot, Bone ingrowth in porous titanium implants produced by 3D fiber deposition, *Biomaterials* 28 (2007) 2810–2820.
- [21] W. Niu, C. Bai, G. Qiu, Q. Wang, Processing and properties of porous titanium using space holder technique, *Mater. Sci. Eng.: A* 506 (2009) 148–151.
- [22] C. Torres-Sanchez, J. McLaughlin, A. Fotticchia, Porosity and pore size effect on the properties of sintered Ti35Nb4Sn alloy scaffolds and their suitability for tissue engineering applications, *J. Alloys Comp.* 731 (2018) 189–199.
- [23] Striker, Tritanium: built to fuse (<http://www.stryker.com/builttofuse/>), 2019.
- [24] Captiva, Tirbinox-c titanium cervical cage (<https://www.captivaspine.com/>), 2019.
- [25] Nuvasi, Modulus titanium technology (<https://www.nuvasive.com/solutions/advanced-materials-science/modulus-titanium-technology/>), 2019.
- [26] M. de Wild, R. Schumacher, K. Mayer, E. Schkommodau, D. Thoma, M. Bredell, A. Kruse Gujer, K.W. Grätz, F.E. Weber, Bone regeneration by the osteoconductivity of porous titanium implants manufactured by selective laser melting: a histological and micro computed tomography study in the rabbit, *Tissue Eng. Part A* 19 (2013) 2645–2654.
- [27] C. Yan, L. Hao, A. Hussein, P. Young, Ti-6Al-4V triply periodic minimal surface structures for bone implants fabricated via selective laser melting, *J. Mech. Behavior Biomed. Mater.* 51 (2015) 61–73.
- [28] X. Cheng, S. Li, L. Murr, Z. Zhang, Y. Hao, R. Yang, F. Medina, R. Wicker, Compression deformation behavior of Ti-6Al-4V alloy with cellular structures fabricated by electron beam melting, *J. Mech. Behavior Biomed. Mater.* 16 (2012) 153–162.
- [29] P.F. Egan, V.C. Gonella, M. Engensperger, S.J. Ferguson, K. Shea, Computationally designed lattices with tuned properties for tissue engineering using 3D printing, *PLoS ONE* 12 (2017) 1–20.
- [30] J. Kaddhodapour, H. Montazerian, A. Darabi, A. Anaraki, S. Ahmadi, A. Zadpoor, S. Schmauder, Failure mechanisms of additively manufactured porous biomaterials: effects of porosity and type of unit cell, *J. Mech. Behavior Biomed. Mater.* 50 (2015) 180–191.
- [31] F. Bobbert, K. Lietaert, A. Eftekhari, B. Pouran, S. Ahmadi, H. Weinans, A. Zadpoor, Additively manufactured metallic porous biomaterials based on minimal surfaces: a unique combination of topological, mechanical, and mass transport properties, *Acta Biomaterialia* 53 (2017) 572–584.
- [32] O. Al-Ketan, R. Rowshan, R.K. Abu, Al-Rub, Topology-mechanical property relationship of 3D printed strut, skeletal, and sheet based periodic metallic cellular materials, *Additive Manuf.* 19 (2018) 167–183.
- [33] E. Alabort, D. Barba, R. Reed, Design of metallic bone by additive manufacturing, *Scripta Materialia* (2019).
- [34] F. Liu, Z. Mao, P. Zhang, D.Z. Zhang, J. Jiang, Z. Ma, Functionally graded porous scaffolds in multiple patterns: new design method, physical and mechanical properties, *Mater. Des.* 160 (2018) 849–860.
- [35] S. Van Bael, Y.C. Chai, S. Truscetto, M. Moesen, G. Kerckhofs, H. Van Oostervyck, J.P. Kruth, J. Schrooten, The effect of pore geometry on the in vitro biological behavior of human periosteum-derived cells seeded on selective laser-melted Ti6Al4V bone scaffolds, *Acta Biomaterialia* 8 (2012) 2824–2834.
- [36] X.Y. Zhang, G. Fang, J. Zhou, Additively manufactured scaffolds for bone tissue engineering and the prediction of their mechanical behavior: A review, *Materials* 10 (2017).
- [37] S. Van Bael, G. Kerckhofs, M. Moesen, G. Pyka, J. Schrooten, J.P. Kruth, Micro-CT-based improvement of geometrical and mechanical controllability of selective laser melted Ti6Al4V porous structures, *Mater. Sci. Eng. A* 528 (2011) 7423–7431.
- [38] D. Wang, Y. Yang, R. Liu, D. Xiao, J. Sun, Study on the designing rules and processability of porous structure based on selective laser melting (SLM), *J. Mater. Processing Technol.* 213 (2013) 1734–1742.
- [39] X.P. Tan, Y.J. Tan, C.S. Chow, S.B. Tor, W.Y. Yeong, Metallic powder-bed based 3D printing of cellular scaffolds for orthopaedic implants: a state-of-the-art review on manufacturing, topological design, mechanical properties and biocompatibility, *Mater. Sci. Eng. C* 76 (2017) 1328–1343.
- [40] D. Melancon, Z. Bagheri, R. Johnston, L. Liu, M. Tanzer, D. Pasini, Mechanical characterization of structurally porous biomaterials built via additive manufacturing: experiments, predictive models, and design maps for load-bearing bone replacement implants, *Acta Biomaterialia* 63 (2017) 350–368.
- [41] M.F. Ashby, R.F.M. Medalist, The mechanical properties of cellular solids, *Metall. Trans. A* 14 (1983) 1755–1769.
- [42] L.J. Gibson, M.F. Ashby, Cellular Solids, Cambridge University Press, Cambridge, 1997 doi:10.1017/CBO9781139878326.
- [43] X.-Y. Zhang, G. Fang, S. Leeftang, A.A. Zadpoor, J. Zhou, Topological design, permeability and mechanical behavior of additively manufactured functionally graded porous metallic biomaterials, *Acta Biomaterialia* 84 (2018) 437–452.
- [44] S. Xu, J. Shen, S. Zhou, X. Huang, Y.M. Xie, Design of lattice structures with controlled anisotropy, *Mater. Des.* 93 (2016) 443–447.
- [45] P.H. Warnke, T. Douglas, P. Wollny, E. Sherry, M. Steiner, S. Galonska, S.T. Becker, I.N. Springer, J. Wiltfang, S. Sivananthan, Rapid prototyping: porous titanium alloy scaffolds produced by selective laser melting for bone tissue engineering, *Tissue Eng. Part C: Methods* 15 (2009) 115–124.
- [46] N. Taniguchi, S. Fujibayashi, M. Takemoto, K. Sasaki, B. Otsuki, T. Nakamura, T. Matsushita, T. Kokubo, S. Matsuda, Effect of pore size on bone ingrowth into porous titanium implants fabricated by additive manufacturing: an in vivo experiment, *Mater. Sci. Eng. C* 59 (2016) 690–701.
- [47] A. Fukuda, M. Takemoto, T. Saito, S. Fujibayashi, M. Neo, D.K. Pattanayak, T. Matsushita, K. Sasaki, N. Nishida, T. Kokubo, T. Nakamura, Osteoinduction of porous Ti implants with a channel structure fabricated by selective laser melting, *Acta Biomaterialia* 7 (2011) 2327–2336.
- [48] S.-H. Wu, Y. Li, Y.-Q. Zhang, X.-K. Li, C.-F. Yuan, Y.-L. Hao, Z.-Y. Zhang, Z. Guo, Porous titanium-6 aluminum-4 vanadium cage has better osseointegration and less micromotion than a poly(ether-ether-ketone) cage in sheep vertebral fusion, *Artificial Organs* 37 (2013) E191–E201.
- [49] H. Götz, M. Müller, A. Emmel, U. Holzwarth, R. Erben, R. Stangl, Effect of surface finish on the osseointegration of laser-treated titanium alloy implants, *Biomaterials* 25 (2004) 4057–4064.

- [50] Y. Kuboki, Q. Jin, H. Takita, Geometry of carriers controlling phenotypic expression in bmp-induced osteogenesis and chondrogenesis, *JBJS* 83 (2001) S105–S115.
- [51] E. Tsuruga, H. Takita, H. Itoh, Y. Wakisaka, Y. Kuboki, Pore size of porous hydroxyapatite as the cell-substratum controls bmp-induced osteogenesis, *J. Biochem.* 121 (1997) 317–324.
- [52] V. Karageorgiou, D. Kaplan, Porosity of 3d biomaterial scaffolds and osteogenesis, *Biomaterials* 26 (2005) 5474–5491.
- [53] Striker, Tritanium pl – posterior lumbar cage, technical summary, 2019.
- [54] Autodesk, Netfabb-ultimate, 2019.
- [55] Materialise, Materialise magics (<https://www.materialise.com/en/software/magics>), 2019.
- [56] S.S. IP, Simpleware – scan ip (<https://www.synopsys.com/simpleware.html>), 2019.
- [57] T. Scientific, 3d visualization & analysis software avizo (<https://www.thermofisher.com/uk/en/home/industrial/electron-microscopy/electron-microscopy-instruments-workflow-solutions/3d-visualization-analysis-software/avizo-materials-science.html>), 2019.
- [58] Q. Chen, G.A. Thouas, Metallic implant biomaterials, *Mater. Sci. Eng.: R: Rep.* 87 (2015) 1–57.
- [59] K. Takamura, K. Hayashi, N. Ishinishi, T. Yamada, Y. Sugioka, Evaluation of carcinogenicity and chronic toxicity associated with orthopedic implants in mice, *J. Biomed. Mater. Res.* 28 (1994) 583–589.
- [60] G.O. Alrabeah, P. Brett, J.C. Knowles, H. Petridis, The effect of metal ions released from different dental implant-abutment couples on osteoblast function and secretion of bone resorbing mediators, *J. Dentistry* 66 (2017) 91–101.
- [61] A. Biesiekierski, J. Wang, M.A.-H. Gepreel, C. Wen, A new look at biomedical ti-based shape memory alloys, *Acta Biomaterialia* 8 (2012) 1661–1669.
- [62] V. Deshpande, N. Fleck, M. Ashby, Effective properties of the octet-truss lattice material, *J. Mech. Phys. Solids* 49 (2001) 1747–1769.
- [63] Y. Li, C. Yang, H. Zhao, S. Qu, X. Li, Y. Li, New developments of ti-based alloys for biomedical applications, *Materials* 7 (2014) 1709–1800.
- [64] W. Murphy, J. Black, G.W. Hastings, *Handbook of Biomaterial Properties*, Springer, 2016.
- [65] O. Lindahl, Mechanical properties of dried defatted spongy bone, *Acta Orthopaedica Scandinavica* 47 (1976) 11–19.
- [66] J.-Y. Rho, T.Y. Tsui, G.M. Pharr, Elastic properties of human cortical and trabecular lamellar bone measured by nanoindentation, *Biomaterials* 18 (1997) 1325–1330.
- [67] G.U. Unnikrishnan, J.A. Gallagher, A.I. Hussein, G.D. Barest, E.F. Morgan, Elastic anisotropy of trabecular bone in the elderly human vertebra, *J. Biomech. Eng.* 137 (2015) 114503.
- [68] E.F. Morgan, H.H. Bayraktar, T.M. Keaveny, Trabecular bone modulus–density relationships depend on anatomic site, *J. Biomech.* 36 (2003) 897–904.
- [69] J.Y. Rho, R.B. Ashman, C.H. Turner, Young's modulus of trabecular and cortical bone material: ultrasonic and microtensile measurements, *J. Biomech.* 26 (1993) 111–119.
- [70] B.V. Rietbergen, A. Odgaard, J. Kabel, R. Huiskes, Direct mechanics assessment of elastic symmetries and properties of trabecular bone architecture, *J. Biomech.* 29 (1996) 1653–1657.
- [71] S. Bondarenko, N. Dedukh, V. Filipenko, M. Akonjom, A.A. Badnaoui, R. Schwarzkopf, Comparative analysis of osseointegration in various types of acetabular implant materials, *HIP Int.* 28 (2018) 622–628 PMID:29742946 .
- [72] F.M. Klenke, Y. Liu, H. Yuan, E.B. Hunziker, K.A. Siebenrock, W. Hofstetter, Impact of pore size on the vascularization and osseointegration of ceramic bone substitutes in vivo, *J. Biomed. Mater. Res. Part A* 85A (2008) 777–786.
- [73] J. Souza, M. Sordi, M. Kanazawa, S. Ravindran, B. Henriques, F. Silva, C. Aparicio, L. Cooper, Nano-scale modification of titanium implant surfaces to enhance osseointegration, *Acta Biomaterialia* (2019).
- [74] F.A. Shah, P. Thomsen, A. Palmquist, Osseointegration and current interpretations of the bone-implant interface, *Acta Biomaterialia* 84 (2019) 1–15.
- [75] W. Zhang, H. Cao, X. Zhang, G. Li, Q. Chang, J. Zhao, Y. Qiao, X. Ding, G. Yang, X. Liu, X. Jiang, A strontium-incorporated nanoporous titanium implant surface for rapid osseointegration, *Nanoscale* 8 (2016) 5291–5301.
- [76] M. Niinomi, Mechanical properties of biomedical titanium alloys, *Mater. Sci. Eng.: A* 243 (1998) 231–236.
- [77] M. Niinomi, Mechanical biocompatibilities of titanium alloys for biomedical applications, *J. Mech. Behavior Biomed. Mater.* 1 (2008) 30–42.
- [78] L. Zhang, D. Klemm, J. Eckert, Y. Hao, T. Sercombe, Manufacture by selective laser melting and mechanical behavior of a biomedical ti–24nb–4zr–8sn alloy, *Scripta Materialia* 65 (2011) 21–24.
- [79] P. Hansma, 2018, AFM and SEM imaging of bone: URL: <https://hansmalab.physics.ucsb.edu/afmbone.html>.
- [80] M. Niinomi, Mechanical properties of biomedical titanium alloys, *Mater. Sci. Eng.: A* 243 (1998) 231–236.